

Article

Investigation on Hydrodynamic Characteristics, Wave–Current Interaction and Sensitivity Analysis of Submarine Hoses Attached to a CALM Buoy

Chiemela Victor Amaechi ^{1,2,*} , Facheng Wang ^{3,*} and Jianqiao Ye ^{1,*}

¹ Department of Engineering, Lancaster University, Lancaster LA1 4YR, UK

² Standards Organisation of Nigeria (SON), 52 Lome Crescent, Wuse Zone 7, Abuja 900287, Nigeria

³ Department of Civil Engineering, Tsinghua University, Beijing 100084, China

* Correspondence: c.amaechi@lancaster.ac.uk (C.V.A.); wangfacheng@tsinghua.edu.cn (F.W.); j.ye2@lancaster.ac.uk (J.Y.)

Abstract: There is an increase in the utilization of the floating offshore structure (FOS) called Catenary Anchor Leg Mooring (CALM) buoys and the attached marine hoses due to the increasing demand for oil and gas products. These hoses are flexible and easier to use but have a short service life of about 25 years. They are adaptable in ocean locations of shallow, intermediate and deep waters. In this research, a numerical model was developed using a coupling method modeled by utilizing ANSYS AQWA and Orcaflex (Orcina Ltd., Ulverston, UK) dynamic models of the CALM buoy hoses. Two cases were comparatively studied: Lazy-S and Chinese-lantern configurations, under ocean waves and current. Comparisons were also made between coupled and uncoupled models. This research presents the hydrodynamic characteristics with a sensitivity analysis on the influence of waves, current attack angle, soil gradient, soil stiffness and environmental conditions that influence the performance of marine hoses. The study comparatively looked at the configurations from dynamic amplification factors (DAF) on marine hoses. The results show that marine hoses can be easily configured to suit the designer's need, seabed soil type, seabed topography and the profiles that are useful for manufacturers. The sensitivity analysis also shows the effect of hose parameters on its hydrodynamic behavior from the wave–current interaction (WCI).

Keywords: ocean wave hydrodynamics; catenary anchor leg mooring (CALM) buoy; Lazy-S configuration; Chinese-Lantern configuration; marine bonded hose; sensitivity; submarine hose; floating hose; hydrodynamics; ocean engineering; bonded marine hoses; marine riser; ocean waves; floating offshore platform (fos); wave–current interaction (WCI)



Citation: Amaechi, C.V.; Wang, F.; Ye, J. Investigation on Hydrodynamic Characteristics, Wave–Current Interaction and Sensitivity Analysis of Submarine Hoses Attached to a CALM Buoy. *J. Mar. Sci. Eng.* **2022**, *10*, 120. <https://doi.org/10.3390/jmse10010120>

Academic Editors: José A.F.O. Correia and Alvise Benetazzo

Received: 19 December 2021

Accepted: 10 January 2022

Published: 17 January 2022

Publisher's Note: MDPI stays neutral with regard to jurisdictional claims in published maps and institutional affiliations.



Copyright: © 2022 by the authors. Licensee MDPI, Basel, Switzerland. This article is an open access article distributed under the terms and conditions of the Creative Commons Attribution (CC BY) license (<https://creativecommons.org/licenses/by/4.0/>).

1. Introduction

In recent times, applications of bonded flexible risers, unbonded flexible risers, composite risers and marine hoses have increased in the marine industry [1–9]. This is due to the need for more flexible offshore platforms and lighter sustainable materials [10–17]. These are utilized for discharging, loading and ocean monitoring. Marine bonded hoses are light conduit structures for fluid transportation from an offshore platform to a Floating Production Storage and Offloading (FPSO) unit/Floating Storage and Offloading (FSO) tanker [18–25]. Since advances into deep-water explorations have increased the need for more sustainable and cost-efficient platforms, these marine structures have received increased attention for their application in offshore loading and offloading operations. Thus, there is a need for Catenary Anchor Leg Mooring (CALM) buoys and other flexible structures. Larger floating offshore structures (FOS), such as Paired Column Semisubmersibles (PCSemis), FPSOs and Very Large Floating Structures (VLFS), do not have such flexibility [26–33]. They also require a larger area on the sea for installation and operation, unlike the CALM buoy hose systems. The classification of marine hoses includes submarine hoses,

reeling hoses and floating hoses [34–41] based on different material and hose design configurations [42–49]. These marine bonded hoses each have different pressure ratings, such as 9 bar, 19 bar and 21 bar ratings. However, these hoses have a short service life of about 25 years; thus, there is a need for more sensitivity studies on the load response behavior of marine bonded hoses, as proposed herein. Secondly, the effect of wave forces on buoys can be some impact on the floater's motion because of the sheer narrow water plane area. Thus, the wave–current interaction (WCI) is pertinent for hydrodynamic sensitivity studies on the buoy-hose system. A typical CALM buoy with turret-design is shown in Figure 1, which is located at Apache Stag Field, Australia, during its installation by Bluewater [49].



Figure 1. CALM Turret buoy at Apache Stag Field, Australia, Buoy during installation (Reprinted with permission from ref. [49]. Copyright 2011 Bluewater).

Studies on the WCI, including the effect of current velocity, have been conducted both on different climatic conditions [50–54] and various FOSs, such as semisubmersible platforms [55,56] and floating wind turbines [57,58], among others. However, the literature search shows no literature has presented the effect of current velocity on the wave forces acting on the CALM buoy motion. Waves, wind and currents are important components of the environmental loads [59–61] on FOSs such as buoys [62–65]. To compute wave forces on offshore structures, wave theories, such as the linear wave theories, Stokes wave theory and Airy wave theory, are utilized [66,67]. Conversely, over the past decades, wave loadings on FOSs have been calculated using linear theory [68,69], second-order wave forces [70–75] and Morison's equation [76–78]. However, due to different constraints, Morison's equation has been modified [76,77]. Morison's equation is used to determine the inertial and drag components of the FOS's body, as well as the body's inertial and drag components [78]. However, Morison's equation is insufficient for evaluating wave forces on offshore constructions, since it ignores wave diffraction. Thus, wave theories that consider diffraction are widely employed. There are limitations to the Morison's equation, since it was proposed by Morison for piles, but it is applicable in various offshore

design formulations particularly marine hoses [78–84]. Many studies on cylinders and piles have led to a better understanding of the hydrodynamics of cylindrical bodies, such as cylindrical FPSOs and cylindrical CALM buoys. MARIN and SOFEC conducted some model tests on CALM buoy motion with recommendations for damping in pitch, heave and roll motions [85,86]. Potential theory has also made it easier to estimate the flow around spheres, buoys and cylinders. Potential theory also defines the fluid domain and wave forces surrounding the subsea marine hose as an offshore structure [87–89]. Bhatta and Rahman [90] used differential equations and Lighthill's [90,91] perturbation approach to produce the boundary conditions, forces and moments of an undersea hose segment, utilizing radiation/diffraction theory. Some reports have found nonlinearities in materials that have also been observed in hose dynamics, and presented with dynamical equations formulated for marine hoses [92–94]. Other mathematical models based on the potential theory on CALM buoy hydrodynamics have also been presented [95–100]. In the offshore industry, the challenges of the incident, scattered and diffraction wave potentials have long been debated. These successfully approached wave theories have been developed to solve some of these issues. Wave forces can generate stress effects due to material complexities, leading to excessive motion predictions, system failures and material breakdowns [101–103]. They could produce substantial deformations, bending and torsional forces in marine hoses. As a result, hydrodynamic sensitivity analysis of the floating structure's motion behavior is required. Validated studies avow that hydrodynamic loads are used to assay the strength of various FOSs, hull designs and components such as composite marine risers and offshore hoses [104–108]. However, wave action has an impact on the motion and strength of CALM buoy hose systems. Wave loads are also considered during hose connection operations, hose riser deployments and hoseline/pipeline installations [109,110]. Based on hydrodynamic sensitivity studies, different sensitivity studies have been conducted for marine hoses and marine risers [111–113]. Pecher et al. [113] conducted sensitivity and comparative studies on CALM and SALM mooring for Wave Energy Converters (WECs). Sun and Wang [114] presented a sensitivity analysis on Lazy-Wave Flexible Riser modeled in ABAQUS to investigate the parameters of the buoyancy modules on the riser. In that study, the outer diameter and position of the buoyancy module were opined as high-sensitivity variables. In addition, the outside diameter had a significant impact on the riser's section moment, whereas the placement had an impact on both section force and section moment. The impact of length on the overall performance of the riser was minimal, according to the research. Amaechi et al. [115] presented a sensitivity study by comparatively looking at the parametric configurations of marine hoses, using a uniquely coupled model developed using Orcaflex's line elements. Bidgoli et al. [116] presented a sensitivity analysis of different deepwater riser configurations modeled with Conventional Mooring Systems (CMS). In their study, three distinct forms of the more commonly utilized deep water risers were chosen and combined with the mooring systems, yielding six alternative case studies modeled in OrcaFlex program. Axelsson and Skjerve [117] investigated the sensitivity of bending and radial gaps on the collapse analyses of flexible riser carcass developed in LS-Dyna and MARC. Sensitivities on straight and curved pipe sections, axially preloaded carcass, carcass ovality, radial gap between carcass and pressure sheets and pressure increase velocity were all part of the investigation. On the tension parameter, Tang et al. [118] investigated the influence of bending, displacement and tension on marine drilling risers in the finite element modeling (FEM) using ABAQUS, whereas Zhang et al. [119] investigated the sensitive effect of top tension on the Vortex-Induced Vibration (VIV) of marine risers in deep waters using computational fluid dynamics (CFD). Other sensitivity investigations have been reported on the fatigue life prediction of risers. These can be seen in a number of sensitivity analyses on Steel Catenary Risers conducted on its Fatigue Behavior [120,121]. In the study by Yang and Li [121], the sensitivity analysis on the fatigue life of Steel Lazy Wave Catenary Risers (SLWR) conducted was motivated by the major consideration encountered while evaluating the practicality of using SLWR on large motion vessels such as semi-submersibles and floating production storage and offloading

(FPSOs) structures. There are other sensitivities in catenary sections and its impact along the touchdown zone [122,123]. Quéau et al. [123] presented some sensitivity investigations on fatigue damage of SCR dynamic loads in the touchdown zone by utilizing a simple stress range evaluation framework. To improve the certainty on the design of SCR attached to deep-water FPSOs, a sensitivity analysis was conducted by Yoo and Joo [124] under 1400 m water depth for deep-water environments in West Africa. Thus, there is a need for an investigation of the hydrodynamic characteristics and the wave–current interaction with the sensitivity studies of the attached hoses and a comparison of the designs for Lazy-S and Chinese-lantern configurations, as performed in this present study.

In the present paper, the hydrodynamic characteristics with the sensitivity studies on CALM buoy with attached marine hoses have been presented. This was carried out using developed numerical marine hose model under ocean environment with wave loads, as introduced in Section 1. Section 2 presents the definition of the problem, the theory with mathematical formulations and the governing equations. Section 3 presents the numerical model of the submarine hoses as attached to a floating CALM buoy structure, under waves and current. Two different representative configurations were applied—the Lazy-S configuration and the Chinese Lantern configuration, as illustrated in Figure 2a,b, respectively. The numerical model was developed using ANSYS AQWA R1 2021 [125,126] and Orcaflex 11.0f [127–129]. Section 4 presents results and discussion, while further discussions on the studies are presented in Section 5. The concluding remarks are given in Section 6.

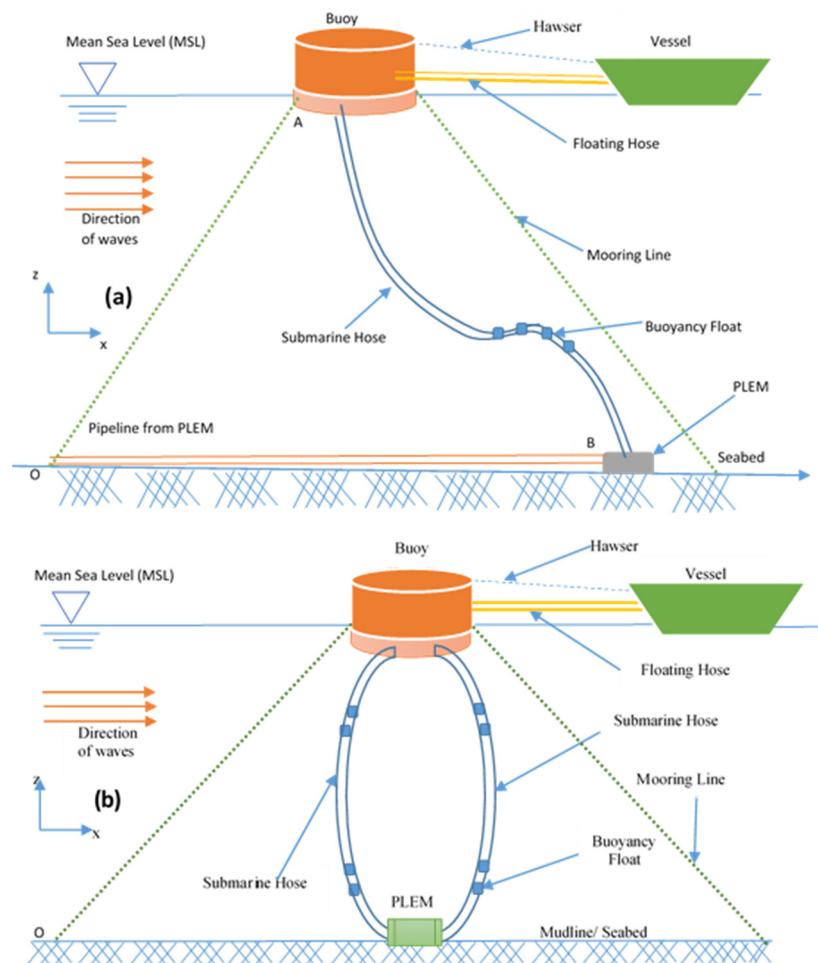


Figure 2. Sketch of the loading and offloading operation on a CALM buoy in (a) Lazy-S and (b) Chinese-Lantern configurations, with wave forces and boundary conditions.

2. Theory and Governing Equations

This section covers the theory of the hydrodynamics aspects for the buoy’s motion, and the response behavior of the attached marine hoses.

2.1. Definition of the Problem

An elastically moored floating buoy of radius a is acted upon by a wave train of irregular waves and wave height H progressing in the x -direction, as shown in Figure 2. The floating buoy is rigid, and is acted upon by propagating waves on a fluid of uniform depth h . The buoy faces up in z -direction, as a fixed coordinate system with x , y and z axes with two submarine hoses connected to it underneath. The floating buoy has two submarine hoses, each of bending stiffness EI and mass per unit length M . One end of the hose-string is connected under the buoy, and the other end is connected to the Pipeline End Manifold (PLEM). The length of the hose-string is considered as semi-infinite, as it is long enough for the wave motions and other exciting forces acting on it. The reference axes are the x and z axes, representing the longitudinal and lateral positions. The displacement made in the x -direction is u , while the displacement made in the z -direction is w .

Based on the wave–structure interaction (WSI), the Laplace Equation formulates the motion’s equation that governs the system. This expression is derived from the Continuity Equation for fluids, as shown below:

$$\frac{\partial u}{\partial x} + \frac{\partial v}{\partial x} + \frac{\partial w}{\partial x} = 0 \tag{1}$$

The motion of the system can be represented by Equation (2). In this equation, the Newtonian Force, F , from the external load of the system as the sum of the inertia force of the system, the viscous damping load and the elastic force components (also called the stiffness load of the system), is expressed:

$$F = Ma + Cv + kx \tag{2}$$

For the incompressible flow as considered here, the Continuity Equation applies, where u , v and w are components of the flow domain:

$$\nabla^2\phi = \frac{\partial^2\phi}{\partial r^2} + \frac{1}{r} \frac{\partial\phi}{\partial r} + \frac{1}{r^2} \frac{\partial^2\phi}{\partial\theta^2} + \frac{\partial^2\phi}{\partial z^2} = 0; \text{ for } a \leq r \leq \infty; -h \leq z \leq \eta; -\pi \leq \theta \leq \pi \tag{3}$$

For irrotational motion, all the vector components of the rotation are equal to zero:

$$\frac{\partial w}{\partial y} - \frac{\partial v}{\partial z} = 0; \frac{\partial u}{\partial z} - \frac{\partial w}{\partial x} = 0; \frac{\partial v}{\partial x} - \frac{\partial u}{\partial y} = 0 \tag{4}$$

The vector components for both the Cartesian coordinates and the Polar coordinates are $u = \frac{\partial\phi}{\partial x}$, $v = \frac{\partial\phi}{\partial y}$, $w = \frac{\partial\phi}{\partial z}$, where the scalar function $\phi(x,y,z)$ are relations used in Equation (4).

Introducing the function ϕ to the Continuity Equation gives the second-order linear differential equation, called the Laplace Transform given in Equation (5):

$$\nabla^2\phi = \frac{\partial^2\phi}{\partial x^2} + \frac{\partial^2\phi}{\partial y^2} + \frac{\partial^2\phi}{\partial z^2} = 0 \tag{5}$$

2.2. Assumptions

The buoy system is considered to be the buoy, the attached submarine hoses and the mooring lines. For this study, the hawser lines and the floating hoses are not included, as such vessel response from other FPSO and transport vessels are not considered. The floating buoy considered in this study has six degrees of freedom (6DoFs), as depicted in Figure 3.

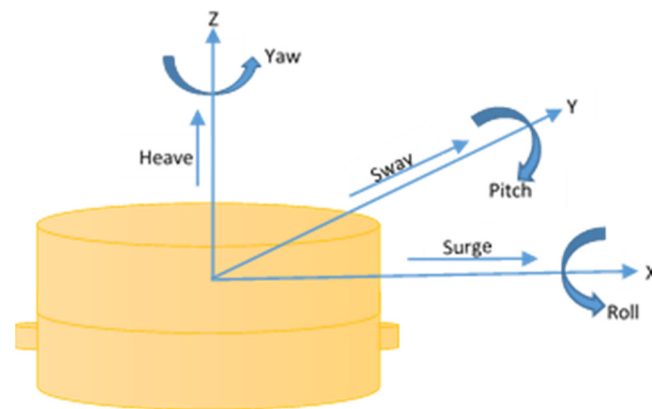


Figure 3. The six degrees of freedom of a floating CALM buoy.

The following assumptions are made:

1. The fluid is incompressible, irrotational and is confined within the ocean's free surface, rigid base and the buoy's surface.
2. The buoy is typically treated as a single system, with a rigid body and 6DoFs.
3. The seabed is horizontally oriented and lies upon a rigid plane. The fluid motion considered in the diffraction analysis is in the cylindrical coordinate system with the format (r, θ, z) .
4. The submarine hose is regarded as a beam that can be bent completely within its limit under pure bending.
5. The hose will be subjected to longitudinal forces due to internal and external forces. However, in depths with minor effects, the outcomes can be very minimal or negligible.
6. The minimum bend radius (MBR) is the inverse of the hose curvature, and the curvature determination can be computed approximately by applying $\frac{1}{r} = \frac{\partial^2 z}{\partial x^2}$. The bend radius of the hose must always be greater than the MBR.
7. Depending on the bending moment, the contribution of both shear pressures and horizontal forces on the curvature is insignificant and can be neglected.
8. There will be some nonlinearities inside the hose originating from the fluids motion due to nonlinearities in the hose geometry.
9. For all cross-sections perpendicular to the hose axis, the hose is treated as a solid body with constant bending stiffness.
10. The hose can also convey (or transport) fluid under high pressure, which can be either oil, gas or water.
11. The hose can be made up of various sections, unfloated sections, floated sections, reinforced ends, flanges and various section radii. The rubber, composite as well as steel components of the hose are considered to have a uniform density, by assumption.
12. The hose was assumed to contain fluid content and to have fully filled up conditions.

2.3. Boundary Condition Formulation

The CALM buoy system's boundary conditions are formulated using the assumptions stated in Section 2.2. Figure 2 depicts a definition sketch of wave forces on a floating buoy in: (a) Lazy-S configuration and (b) Chinese-Lantern configuration. Both configurations have two submarine hoses attached beneath the buoy. The submarine hoses are attached to the bottom by a fixed connection to the PLEM, and the buoy is cylindrical in shape. The seabed is assumed to be horizontal and level (or plane). In the initial boundary condition (IVC) formulation, simplicity was considered. Thus, the mooring lines were not considered, as it reduces complexities in the problem. The boundary conditions are formulated using potential theory, as presented in this section. Equation (1), which is the Laplace transform derived from the continuity equation of fluids, governs the system's motion. Equation (2)

is related to the following boundary conditions. The following boundary conditions are considered:

(a) Dynamic Boundary Conditions:

$$\frac{\partial \phi}{\partial t} + g\eta + \frac{1}{2} \left\{ \left(\frac{\partial \phi}{\partial r} \right)^2 + \left(\frac{1}{r} \frac{\partial \phi}{\partial \theta} \right)^2 + \left(\frac{\partial \phi}{\partial z} \right)^2 \right\} = 0; \text{ for } r \geq a; z = \eta(x, y, t) \quad (6)$$

(b) Kinematic Boundary Conditions:

$$\frac{\partial \eta}{\partial t} + \left(\frac{\partial \phi}{\partial r} \right) \left(\frac{\partial \eta}{\partial r} \right) + \frac{1}{r^2} \left\{ \left(\frac{\partial \phi}{\partial \theta} \right) \left(\frac{\partial \eta}{\partial \theta} \right) \right\} = \frac{\partial \phi}{\partial z}; \text{ for } r \geq a; z = \eta(x, y, t) \quad (7)$$

(c) Free Surface Boundary Conditions:

$$z = \eta(x, y, t) \quad (8)$$

where $z = \eta(x, y, t)$ represents the free surface [80]. The free surface boundary conditions are given in Equations (6) and (7), which are to be satisfied by both the wave elevation η and velocity potential ϕ .

(d) Body Surface Boundary Conditions:

$$\frac{\partial \phi}{\partial r} = 0; \text{ for } r = a; -h \leq z \leq \eta \quad (9)$$

(e) Seabed (or bottom) Boundary Conditions:

For an impermeable seabed of depth $h(x, y)$, carrying a floating buoy, the seabed boundary condition is given by Equation (10):

$$\frac{\partial \phi}{\partial z} = 0; \text{ for } z = -h \quad (10)$$

(f) Radiation Boundary Conditions:

Assuming at infinity, the radiation boundary condition is given by Equation (9), where ϕ_I is the incident wave potential and ϕ_S is the scattered wave potential for this condition:

$$\phi(r, z, t) = \text{Re} \left[\phi(r, z) e^{i\sigma t} \right] = \text{Re} \left[\left(\phi_I + \phi_S e^{i\sigma t} \right) \right] \quad (11)$$

Thus, Equations (15) and (16) will satisfy the radiation potential at infinity:

$$\lim_{kr \rightarrow \infty} \sqrt{kr} \left(\left(\frac{\partial}{\partial r} \right) \pm ik \right) \phi_S = 0; i = \sqrt{-1} \quad (12)$$

$$\lim_{kr \rightarrow \infty} \sqrt{kr} \left(\left(\frac{\partial}{\partial r} \right) \pm ik \right) (\phi - \phi_I) = 0; i = \sqrt{-1} \quad (13)$$

2.4. Wave Exciting Forces

Background on waves, currents and wave theories can be found in the literature, with definitions for the parameters as follows: the wave length, λ , is a function of the wave number, C is the wave Celerity and T is the wave period, given by the expressions $C = \lambda/T$ and $k = 2\pi/\lambda$ [66,67]. Second-order wave loading contributions to the flow domain are made by slender bodies, such as risers, hose-strings, piles and mooring lines. The influence of the theory on big vertical cylinders has been discussed in the literature review in Section 1. These qualities, in theory, influence the behavior of a structure in an ocean body or a water body. Equations (15) and (16) are derived from the Taylor series expansion of the Perturbation Series equation for higher-order corrections [87–91].

The formulation of the wave forces on the submarine hose attached to the CALM buoy may be obtained using an equilibrium equation for the force components. An expression for the total forces is presented in Equation (14), where F is the total force, F_l is the linear

force component, F_s is the second-order force component (for the dynamic force, F_d , and waterline force, F_w , components) and F_q is the quadratic force component:

$$F = F_l + F_s + F_q \tag{14}$$

The wave exciting forces on a CALM buoy have been found by Wang and Sun [130] as expressed in Equations (15) and (16), where S_B is the mean wetted surface of the CALM buoy, n_x is the x -component of the normal vector and n_z is the z -component of the normal vector. Thus:

$$F_x = \iint_{S_B} -P(r, \theta, z, t)n_x ds = f_{x0}e^{-i\omega t} \tag{15}$$

$$F_z = \iint_{S_B} -P(r, \theta, z, t)n_z ds = f_{z0}e^{-i\omega t} \tag{16}$$

2.5. Pressure Distribution

The pressure distribution for the irrotational flow is obtained from Bernoulli’s equation, as given in Equation (17):

$$\frac{P}{\rho} + g\eta + \frac{\partial\phi}{\partial t} + \frac{1}{2} \left\{ \left(\frac{\partial\phi}{\partial r} \right)^2 + \left(\frac{1}{r} \frac{\partial\phi}{\partial\theta} \right)^2 + \left(\frac{\partial\phi}{\partial z} \right)^2 \right\} = 0; \text{ for } r \geq a; z = \eta(x, y, t) \tag{17}$$

Considering the above equations, we obtain the dynamic pressure distribution, the hydrostatic pressure distribution and the transient pressure distribution. Mathematically, these are as follows:

- (a) The dynamic pressure distribution is given by Equation (18), where ρ is the density of the fluid, U_f is the velocity of the fluid, which fluctuates as a result of pressure distributions within the fluid, and Q_f is the speed of the fluid at a given point, f :

$$P_d = \frac{1}{2}\rho(U_f^2 - Q_f^2) \tag{18}$$

- (b) The hydrostatic pressure distribution is given by Equation (19), where P_0 is the hydrostatic pressure, g is acceleration due to gravity, ρ is the density of the fluid and z is the water depth above the level $z = 0$:

$$P_0 = -\rho gz \tag{19}$$

- (c) The transient pressure distribution is given by Equation (20), where ρ is density of fluid, ϕ is the velocity potential while t is the time function:

$$P_t = -\rho \frac{\partial\phi}{\partial t} \tag{20}$$

The total of these pressure distributions acting on a stream of fluid is given by Equation (21). From $\nabla^2\phi$ in Equation (22), we can obtain the pressure distribution as:

$$\frac{P}{\rho} + g\eta + \frac{\partial\phi}{\partial t} + \frac{1}{2}\{(\nabla\phi)^2\} = 0; \text{ for } r \geq a; z = \eta(x, y, t) \tag{21}$$

$$\frac{P}{\rho} + gz + \frac{\partial\phi}{\partial t} + \frac{1}{2}\{(\nabla\phi)^2\} = 0 \tag{22}$$

The derivatives for the fluid velocity is given by the scalar function $\phi(x,y,z)$ with the following relations presented in Equation (23):

$$u = \frac{\partial\phi}{\partial x} = \frac{\partial x}{\partial t}, v = \frac{\partial\phi}{\partial y} = \frac{\partial y}{\partial t}, w = \frac{\partial\phi}{\partial z} = \frac{\partial z}{\partial t} \tag{23}$$

From Equation (21), the total derivative with respect to time, t , can be obtained as:

$$\frac{d}{dt}\left(\frac{P}{\rho}\right) + g\frac{d\eta}{dt} + \frac{d}{dt}\left(\frac{\partial\phi}{\partial t}\right) + \frac{1}{2}\frac{d}{dt}(\nabla\phi)^2 = 0; \text{ for } r \geq a; z = \eta(x, y, t) \quad (24)$$

By considering the condition for the fluid domain at time, t , with the speed of the fluid, $Q = (u, v, w)$, we can obtain Equation (25):

$$\frac{d}{dt}\left(\frac{P}{\rho}\right) + \left[\frac{\partial^2\phi}{\partial t^2} + g\frac{\partial\phi}{\partial\eta}\right] + \frac{d}{dt}(\nabla\phi)^2 + \frac{1}{2}Q\nabla(\nabla\phi)^2 = 0; \text{ for } r \geq a; z = \eta(x, y, t) \quad (25)$$

When the pressure is equal to the atmospheric pressure, $P = P_a$;

$$\frac{d}{dt}\left(\frac{P_a}{\rho}\right) + \left[\frac{\partial^2\phi}{\partial t^2} + g\frac{\partial\phi}{\partial\eta}\right] + \frac{d}{dt}(\nabla\phi)^2 + \frac{1}{2}Q\nabla(\nabla\phi)^2 = 0; \text{ for } r \geq a; z = \eta(x, y, t) \quad (26)$$

At constant atmospheric pressure, P_a ; the first term in Equation (26) limits to zero:

$$\frac{\partial^2\phi}{\partial t^2} + g\frac{\partial\phi}{\partial\eta} + \frac{d}{dt}(\nabla\phi)^2 + \frac{1}{2}Q\nabla(\nabla\phi)^2 = 0; \text{ for } r \geq a; z = \eta(x, y, t) \quad (27)$$

From Equation (27), using only first- and second-order terms in the variable ϕ , we get:

$$-\frac{\partial}{\partial t}(\nabla\phi)^2 = \frac{\partial^2\phi}{\partial t^2} + g\left(\frac{\partial\phi}{\partial z}\right) \quad (28)$$

Lighthill [90] showed that a combination of the two Equations will produce Equation (28). Using polar coordinates, the pressure of the fluid can be obtained from the linear Bernoulli equation in an unsteady state, as given in Equation (29):

$$P(r, \theta, z, t) = -\rho\frac{\partial\phi(r, \theta, z, t)}{\partial t} \quad (29)$$

2.6. Characteristic Value

Characteristic value situations have been used in the past to solve stability problems associated with hydrodynamics. From the equations for the system idealized for the Boundary Value Problem (BVP), it is observed that nonlinearities in the system have been simplified mathematically in the boundary conditions in Section 2.3. This presents the following order for each of the terms in their respective order. The characteristic values can be used to represent each of the terms to simplify the complex situation. The characteristic value problem, or the eigenvalue problem, is shown in Equation (30), where T is the characteristic value of ϕ and λ is the characteristic vector of T :

$$\phi T = \lambda \delta \quad (30)$$

Let us assume that the characteristic wave time period = T , the characteristic wavelength = λ , the characteristic velocity potential = ϕ and the characteristic water depth = δ . By considering the first boundary condition given as Equation (9) in the Cartesian coordinate system, we have the following:

$$\frac{\partial\phi}{\partial t} + g\delta + \frac{1}{2}\left\{\left(\frac{\partial\phi}{\partial x}\right)^2 + \left(\frac{1}{r}\frac{\partial\phi}{\partial y}\right)^2 + \left(\frac{\partial\phi}{\partial z}\right)^2\right\} = 0; \quad (31)$$

Applying the characteristic values for the individual components in Equation (32):

$$\frac{\phi}{T} : \delta : \frac{\lambda}{T^2} : \frac{\phi^2}{\lambda^2} : \frac{\phi^2}{\lambda^2} : \frac{\phi^2}{\lambda^2} \quad (32)$$

Multiply each term by $T^2/\lambda\delta$, we have the following:

$$\frac{\phi}{T} \cdot \frac{T^2}{\lambda\delta} : \delta \cdot \frac{\lambda}{T^2} \cdot \frac{T^2}{\lambda\delta} : \frac{\phi^2}{\lambda^2} \cdot \frac{T^2}{\lambda\delta} : \frac{\phi^2}{\lambda^2} \cdot \frac{T^2}{\lambda\delta} : \frac{\phi^2}{\lambda^2} \cdot \frac{T^2}{\lambda\delta} \tag{33}$$

Simplifying this further, we get the following:

$$\frac{\phi T^2}{T\lambda\delta} : 1 : \frac{\phi^2 T^2}{\lambda^2 \lambda\delta} : \frac{\phi^2 T^2}{\lambda^2 \lambda\delta} : \frac{\phi^2 T^2}{\lambda^2 \lambda\delta} \tag{34}$$

$$\frac{\phi T^2}{T\lambda\delta} : 1 : \frac{\phi^2 T^2}{\lambda^3 \delta} : \frac{\phi^2 T^2}{\lambda^3 \delta} : \frac{\phi^2 T^2}{\lambda^3 \delta} \tag{35}$$

$$\frac{\phi T^2}{T\lambda\delta} : 1 : \left(\frac{\phi^2 T^2}{\lambda^3 \delta}\right)^3 \tag{36}$$

If we take $\frac{\phi T}{\lambda\delta} = 0$ (1), which means that $\phi T = 0(\lambda\delta)$, and $\phi^2 T^2 = 0(\lambda^2 \delta^2)$, this can be expressed in this form:

$$\frac{\phi^2 T^2}{\lambda^3 \delta} = 0\left(\frac{\lambda^2 \delta^2}{\lambda^3 \delta}\right) \tag{37}$$

$$0\left(\frac{\delta}{\lambda}\right) = 0(\epsilon) \tag{38}$$

By considering Equation (31) in the Cartesian coordinate system:

$$\frac{\partial \phi}{\partial z} = \frac{\partial z}{\partial t} + \left(\frac{\partial \phi}{\partial x}\right) \left(\frac{\partial z}{\partial x}\right) + \frac{1}{r^2} \left\{ \left(\frac{\partial \phi}{\partial y}\right) \left(\frac{\partial z}{\partial y}\right) \right\} \tag{39}$$

$$\frac{\partial \phi}{\partial z} = \frac{\partial z}{\partial t} + \left(\frac{\partial \phi}{\partial x} \frac{\partial z}{\partial x}\right) + \left(\frac{\partial \phi}{\partial y} \frac{\partial z}{\partial y}\right) \tag{40}$$

Thus, applying the characteristic values, we have the following:

$$\frac{\phi}{\lambda} : \frac{\delta}{T} : \frac{\delta \phi}{\lambda^2} : \frac{\delta \phi}{\lambda^2} \tag{41}$$

Multiply each term by λ/ϕ , we have the following:

$$1 : \frac{\delta \lambda}{T\phi} : \frac{\phi}{\lambda} : \frac{\phi}{\lambda} \tag{42}$$

Recall that we can take $\frac{\lambda\delta}{\phi T} = 0$ (1), which means that $\lambda\delta = 0(\phi T)$ and $\lambda^2 \delta^2 = 0(\phi^2 T^2)$; therefore, we can have it in this form:

$$1 : 1 : \frac{\phi}{\lambda} : \frac{\phi}{\lambda} \tag{43}$$

$$1 : 1 : \epsilon : \epsilon \tag{44}$$

However, the wave number is $k = 2\pi/\lambda$ and the wave amplitude is $\delta = H/2$. Hence, the constant ϵ can be approached as real, with the following relationship:

$$\epsilon = \frac{kH}{2} \text{ where } \epsilon \leq 1 \tag{45}$$

Comparing Equations (15) and (16), there is a pattern that is consistent for the nonlinear terms in Equations (43) and (44). For each of the boundary conditions, the order ϵ shows a small quantity that is less than or equal to 1, as depicted in Equation (45).

2.7. Perturbation Method

Considering the perturbations (disturbances) in the system, we can represent their sources using the Perturbation method. Thus, the ordinary equations can be represented by η_l, ϕ_l and P_l , while the quadratic solutions can be represented by η_q, ϕ_q and P_q :

$$\phi = \phi_l + \phi_q + \dots \tag{46}$$

$$\eta = \eta_l + \eta_q + \dots \tag{47}$$

$$P = P_l + P_q + \dots \tag{48}$$

The Perturbation method is, thus, applied to solve these BVP as in Section 2.3. The complete form of the equations is first presented, and then we assume that the solution can be represented in the form of a small parameter ϵ . This is solved using the power series expansion method. In that vein, we expand the terms η, ϕ and P , in the power of ϵ . Therefore, these can be represented as:

$$\phi = \sum_{n=1}^{\infty} \epsilon^n \phi_n \tag{49}$$

$$\eta = \sum_{n=1}^{\infty} \epsilon^n \eta_n \tag{50}$$

$$P = \sum_{n=1}^{\infty} \epsilon^n P_n \tag{51}$$

Consider the condition at free surface, $z = \eta(x, y, t)$ from Equation (8). We can substitute the value for free surface condition in the Equation (52):

$$\phi(x, y, z, t) = \phi(x, y, \eta(x, y, t), t) \tag{52}$$

Applying the Taylor Series Expansion when the sea depth is $z = 0$ and atmospheric pressure is $P_o = 0$:

$$\phi(x, y, z, t) = \phi(x, y, (0), t) + \eta \left(\frac{\partial \phi}{\partial z} \right)_{z=0} + P \left(\frac{\partial \phi}{\partial z} \right)_{z=0} + \dots \tag{53}$$

$$\phi(x, y, z, t) = (\phi_l + \phi_q + \dots) + (\eta_l + \eta_q + \dots) \left(\frac{\partial \phi_l}{\partial z} + \frac{\partial \phi_q}{\partial z} + \dots \right)_{z=0} + \dots \tag{54}$$

$$\phi = \phi_l + \phi_q + \eta \left(\frac{\partial \phi}{\partial z} \right)_{z=0} \dots + HOT \tag{55}$$

where *HOT* refers to the higher order terms in the relationship, in the form of ϕ_l for first-order terms and $[\phi_q + \eta \left(\frac{\partial \phi}{\partial z} \right)_{z=0}]$ for the second-order terms. Following the earlier expressions for the Laplace Equation, the differential equations for the potential and pressure terms are obtained:

$$\nabla^2 \phi = \frac{\partial^2 \phi_n}{\partial x^2} + \frac{\partial^2 \phi_n}{\partial y^2} + \frac{\partial^2 \phi_n}{\partial z^2} = 0 \tag{56}$$

$$\nabla^2 \eta = \frac{\partial^2 \eta_n}{\partial x^2} + \frac{\partial^2 \eta_n}{\partial y^2} + \frac{\partial^2 \eta_n}{\partial z^2} = 0 \tag{57}$$

$$\nabla^2 P = \frac{\partial^2 P_n}{\partial x^2} + \frac{\partial^2 P_n}{\partial y^2} + \frac{\partial^2 P_n}{\partial z^2} = 0 \tag{58}$$

Following the same steps for the Taylor Series expansion, Equation (40) can be expanded to obtain the first-order and second-order expressions:

$$\frac{\partial \phi}{\partial z} = \frac{\partial \phi_l}{\partial z} + \frac{\partial \phi_q}{\partial z} + \eta_l \frac{\partial}{\partial z} \left(\frac{\partial \phi_l}{\partial z} \right)_{z=0} + \dots \tag{59}$$

$$\frac{\partial^2 \phi}{\partial z^2} = \frac{\partial^2 \phi_l}{\partial z^2} + \frac{\partial^2 \phi_q}{\partial z^2} + \eta_l \frac{\partial}{\partial z} \left(\frac{\partial^2 \phi_l}{\partial z^2} \right)_{z=0} + \dots \tag{60}$$

2.8. Velocity Potential

Let us consider the fluid domain around the submarine hoses as illustrated in Figure 2. Assume we have sectioned the regions of fluid domain around the CALM buoy by dividing it into three sections denoted by Ω_1 , Ω_2 and Ω_1 . The velocity potential ϕ , which satisfies the boundary conditions given in Section 2.3, is given by the expression:

$$\phi(r, \theta, z) = \sum_{p=0}^{\infty} \varepsilon_p i^p \cos p \theta \cdot \phi_l^p(r, z) \tag{61}$$

where $\varepsilon_0 = 1$, $\varepsilon_p = 2$ and $m \geq 2$

In the outer region, we may represent the velocity potential as follows:

$$\begin{aligned} \phi(r, \theta, z) = & J_p(i\mu_0 r) \cos(\mu_0 z) + A_{p0} \frac{H_p^{(1)}(i\mu_0 r)}{H_p^{(1)'}(i\mu_0 r)} \cos(\mu_0 z) \\ & + \sum_{p=0}^{\infty} A_{pq} \frac{H_p^{(1)}(i\mu_0 r)}{H_p^{(1)'}(i\mu_0 r)} \cos(\mu_0 z) \end{aligned} \tag{62}$$

$$\begin{aligned} \phi(r, \theta, z) = & J_p(i\mu_0 r) \cos(\mu_0 z) + A_{p0} \frac{H_p^{(1)}(i\mu_0 r)}{H_p^{(1)'}(i\mu_0 r)} \cos(\mu_0 z) + \\ & \sum_{p=0}^{\infty} \varepsilon_p i^p \cos p \theta \cdot \phi_l^p(r, z) \mu + H_p(i\mu_0 r) + \cos(\mu_0 z) \end{aligned} \tag{63}$$

3. Materials and Methods

The numerical modeling aspect has been presented in this section on the materials applied in this numerical model and the methodology. The materials include the buoy, submarine hoses, mooring lines and floats, as discussed in the subsequent sub-sections.

3.1. Buoy and Skirt Model

The details for the buoy considered in this research are presented in Table 1. The hydrodynamics, hydrostatics and motion response of the CALM buoy was carried out for the cylindrical buoy (CB). The buoy’s geometry was numerically developed using a Computer-Aided Design (CAD) software called Solidworks 2021 (Dassault Systèmes SOLIDWORKS Corporation, Waltham, MA, USA). The description of the buoy geometry for the first concept of the CALM Buoy and skirt, showing (a) an isometric view and (b) a plan view, is shown in Figure 4. This research also included a comparative study between different geometrical concepts and skirt concepts, but this paper is limited to one concept, as described herein, to present the advantage and justification. One vital use of this includes aiding designers in the consideration of design parameters. The description for the buoy geometry shows the diameters, heights and locations of each part. It includes the CALM buoy body diameter D_B and the CALM buoy skirt diameter D_S , the height of the buoy, H_B , the height of the skirt, H_S , and the height from the keel to the underneath of the skirt, H_K . The model of the CALM buoy in Orcaflex is shown in Figure 5.

Table 1. Parameters of the buoy.

Description	Value	Unit
Buoy Height	4.50	m
Draft	2.40	m
Water Depth	100.00	m
Buoy Mass	19,883,400	kg
Diameter of Buoy body	10.00	m
Diameter of Buoy Skirt	13.90	m

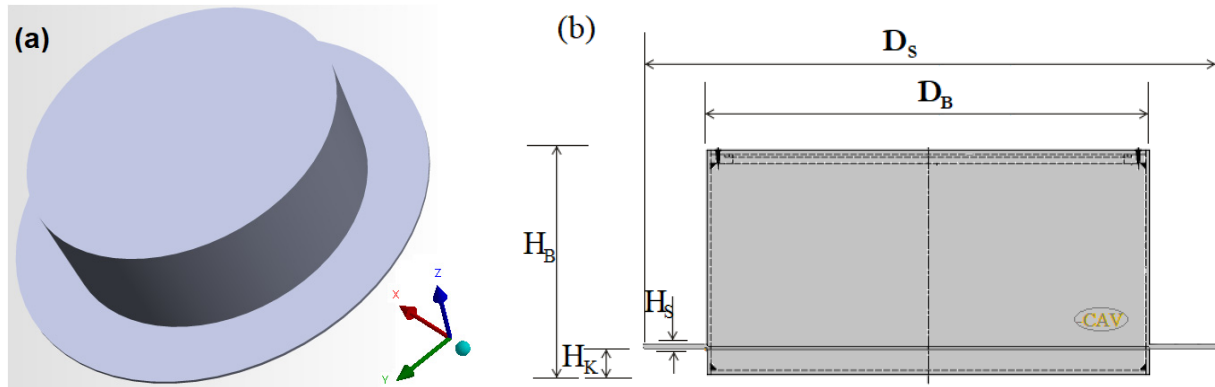


Figure 4. Description of the geometry for the first concept of CALM Buoy and skirt, showing (a) an isometric view and (b) a plan view.

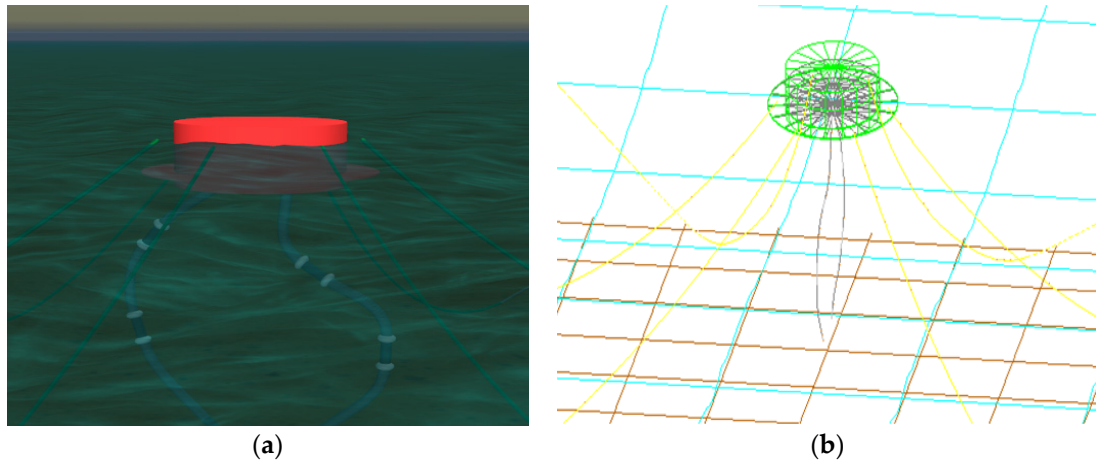


Figure 5. Numerical model of the CALM Buoy showing (a) shaded and (b) wireframe views.

3.2. Submarine Hoses

The modeling consideration on the offshore submarine hose design were for an operation application with pressure rating of 19 bar (1900 KN/m²). The offshore submarine hose was developed and modeled for two cases—Lazy-S and Chinese-lantern configuration, as illustrated in Figure 2a,b. In each case, the two (2) submarine hose-strings are connected to the base of the buoy at the top and the Pipeline End Manifolds (PLEMs) at the bottom. The hoses are designed using existing current practices by hose manufacturers and industry end-users on oil fields [18,19,40–49]. For the Chinese-lantern configuration, the length of both submarine hose-strings was 25.90 m per hose-string, as presented in Table 2. For the Lazy-S configuration, the length of each submarine hose was 162.065 m, as presented in Table 3. The hose was assumed to be filled up and to contain completely full fluid content. For the fluid content, it was tested with sea water with a density of 1025 kg/m³ and with

heavy oil with a density of 825 kg/m³. Details of the parameters for the submarine hose considered is given in Table 2. The section profile for the submarine hose in Orcaflex 11.0f is depicted in Figure 6.

Table 2. Parameters for the submarine hose for Chinese-Lantern configuration with section details arrangement.




Particulars	Description and Value			Unit
	Name	First-off Buoy hose	Mainline hose	
Position of Part	1st Section	2nd Section	3rd Section	-
Hose Type Illustration				-
Hose Body Array	V1 (Hose Fitting)	V2 (Hose Fitting)	V3 (Hose Fitting)	-
	V1 (Reinforced end)	V2 (Hose End)	V3 (Hose End)	-
	V1 (Hose Body)	V2 (Hose Body)	V3 (Hose Body)	-
		V2 (Hose End)	V3 (Reinforced end)	-
		V1 (Hose Fitting)	V2 (Hose Fitting)	V3 (Hose Fitting)
Hose Section Mass	239.00	495.00	239.00	kg/m
Hose Outer Diameter, OD	0.67	0.65	0.67	m
Hose Inner Diameter, ID	0.49	0.49	0.49	m
Hose Length, L	8.40	9.00	8.50	m

Table 3. Parameters for the submarine hose for Lazy-S configuration with section details arrangement.

Section Number	Sub-Sections	Particulars	Inner Diameter (m)	Outer Diameter (m)	Section Length (m)	Segment Length (m)	Number of Segments	Unit Mass (kg/m)	Volume (m ³)	Segment Weight (N)
Hose Group 1: Section 1	1	Fitting	0.489	0.650	1.0	0.800	1	495	0.330	492.5
	2	Reinforced Hose End	0.489	0.650	0.2	3.000	15	239	1.002	721.5
	3	Hose Body	0.489	0.650	0.5	3.236	6	180	1.074	582.5
	4	Hose End	0.489	0.675	0.5	0.895	2	200	0.320	179.0
	5	Fitting	0.489	0.650	1.0	0.800	1	495	0.330	492.5
Hose Group 2: Section 2–Section 20 (same)	6	Fitting	0.489	0.650	1.0	0.800	1	495	0.330	492.5
	7	Hose End	0.489	0.675	0.5	0.895	2	200	0.320	179.0
	8	Hose Body	0.489	0.650	0.2	3.840	19	180	1.274	691.2
	9	Hose End	0.489	0.675	0.5	0.895	2	200	0.320	179.0
	10	Fitting	0.489	0.650	1.0	0.800	1	495	0.330	492.5
Hose Group 3: Section 21	11	Fitting	0.489	0.650	1.0	0.800	1	495	0.330	492.5
	12	Hose End	0.489	0.675	0.5	0.895	2	200	0.320	179.0
	13	Hose Body	0.489	0.650	0.5	3.236	6	180	1.074	582.5
	14	Reinforced Hose End	0.489	0.670	0.2	3.000	15	240	1.064	724.6
	15	Fitting	0.489	0.650	1.0	0.800	1	495	0.330	492.5

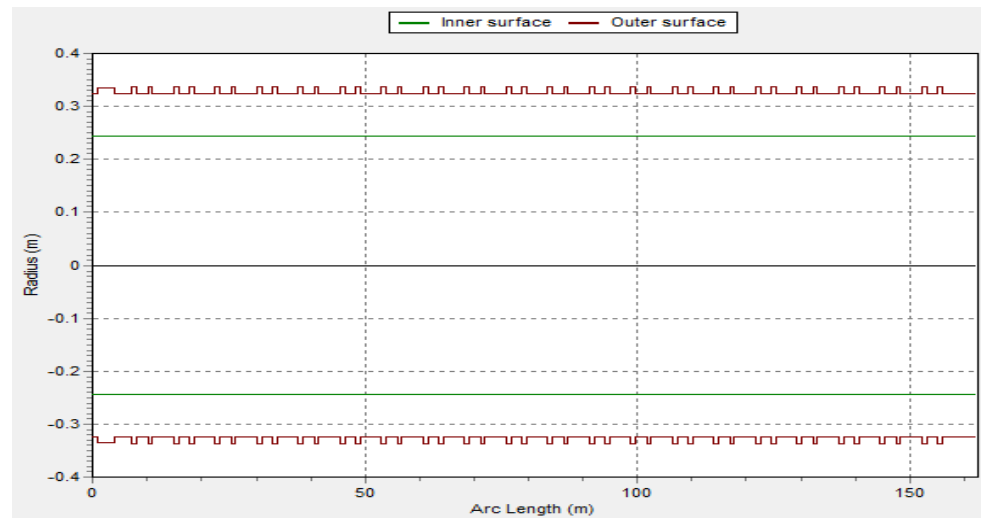


Figure 6. Submarine hose profile showing the radii for inner and outer surfaces in Orcaflex.

3.3. Mooring Lines

The mooring arrangement is 6 mooring lines positioned strategically at 60° separation distance apart, to avoid line clashing. The schematic for the two configurations investigated are presented in Figures 2 and 7. Details of the mooring line parameters are detailed in Table 4. Each of the mooring lines have the same stiffness. They are deployed as catenary mooring lines. For the arrangement, each mooring line is made up of two sections of steel chains. Two different materials were investigated on the mooring lines using steel chain and polyester mooring lines. Additionally, two different configurations for the section ratio were used: 150:195 and 50:175. The 2.5" mooring chain has a mass per unit length of 0.088 te/m (te: metric tonne). In Orcaflex [127–129], the bending stiffness is set to zero for both the studlink and the studless chains. In Table 4, C_m denotes the inertia coefficient, which is related to C_a , the added mass coefficient, using the empirical relationship in [127], as $C_m = 1 - C_a$.

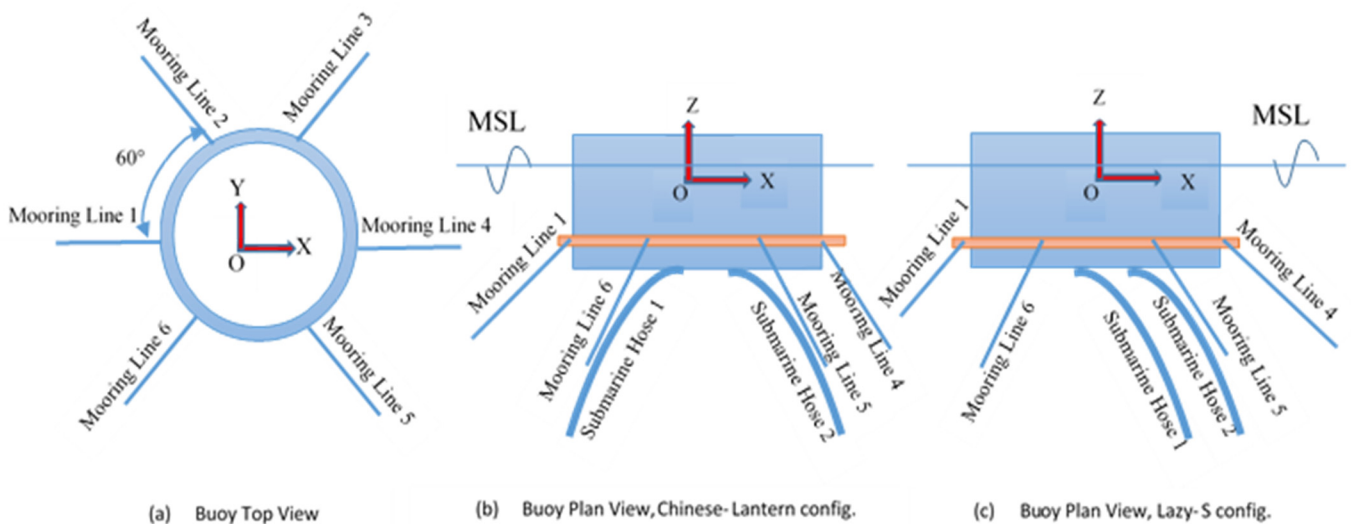


Figure 7. Schematic for the moorings on the buoy showing.

Table 4. Parameters for the mooring lines.

Description	Value	Unit
Coefficient of Drag, C_d	1.00	-
Coefficient of Inertia, C_m	1.00	-
Section Lengths Ratio for the first config.	150:195	-
Section Lengths Ratio for the second config.	50:175	-
Poisson Ratio	0.50	-
Mass Per Unit Length	0.088	te/m
Contact Diameter	0.229	m
Nominal Diameter	0.120	m
Bending Stiffness	0.00	N·m ²
Axial Stiffness, EA	407,257.00	kN
Separation Angle between lines	60	Degrees (°)

3.4. Buoyancy Float

With a float incorporated as part of the hose line, the buoyancy connection on the hoses was designed. The design of the float materials is constructed as shown in Table 5, in accordance with the OCIMF (Oil Companies International Marine Forum) industry requirements [19,34–36]. The buoyancy of the submarine hose line is obtained by designing a series of floats arranged together, as depicted in Figure 8.

Table 5. Parameters for the buoyancy floats.

Item	Value	Item	Value
Classification of Float	Standard float	Unit Mass, w (kg)	102.00
Float Type	Bolted type	Net Buoyancy, b_f (kg)	280.00
Filling Material	Polyurethane foam	Outer Diameter, D_o (m)	1.23
Metal Part Material	Stainless Steel	Inner Diameter, D_f (m)	0.799
Shell Material	Polyethylene	Length of Float, L_f (m)	0.60
Number of floats	Depends on config.	Pitch of Floats, S_f (m)	2.00

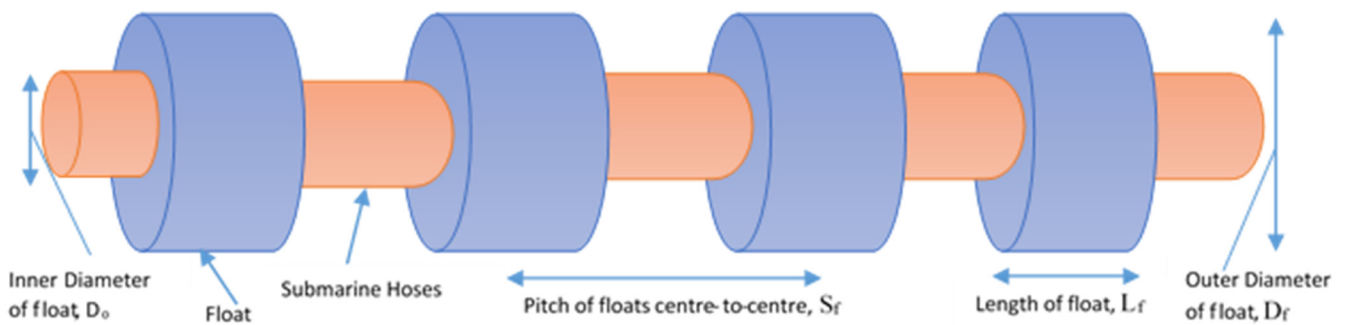


Figure 8. Typical floats attached to offshore submarine hoses.

In principle, submarine hoses are classified as slender bodies, and the floats are usually attached on them. The damping for the submarine hose can be evaluated by applying the modified Morison Equation [78], given in Equation (3), where D is the diameter of the body, V is the volume of the body, V_r is the relative velocity of fluid particles, A is the area of the body, C_a is the added mass coefficient, C_d is the drag coefficient and C_m is the inertial force coefficient:

$$F = \rho V \dot{u} + \rho C_a D A (V_r) + \frac{1}{2} \rho C_d A (V_r) |V_r| \tag{64}$$

However, for the floats, the principle of hydrodynamic equivalence is applied. With the application of the equivalence principle of the hydrodynamic loads per unit length and buoyancy load for the buoyancy section, as presented in [131], the expression for the equivalent float weight w_e , equivalent float outer diameter D_e , and equivalent hydrodynamic

coefficients C_{de} and $C_{\tau e}$ for the buoyancy section can be presented as in Equations (66)–(68), where w is the weight per unit length of riser, l_f is the length of float, v_f is the volume of float, S_f is the float pitch, ρ_f is the material density of buoyancy block, m_f is the mass of float line considered, F_{df} is the damping force of float, m_{ft} is the mass of attached rigging hardware of buoyancy float block (such as bolts, fixing clamps, etc.), D_{ol} is the outer diameter of the derived hoseline and $C_{\tau n}$ is the tangential drag coefficient acting on the cross section of buoyancy float block. The equivalent normal and tangential added mass coefficients for the buoyancy section can refer to the equivalent process of drag force coefficients [127–129]. The drag force per unit length of the derived hoseline, F_{df} , when the flow is normal to the line’s axis along the local x-direction is given by Equation (65):

$$F_{df} = \frac{1}{4} [\rho_f V_f^2 C_{df} (D_f^2 - D_o^2)] \tag{65}$$

$$D_e = \sqrt{(D_f^2 - D_o^2) \cdot (L_f/S_f) + D_o^2} \tag{66}$$

$$C_{de} = \frac{C_d}{D_e S_f} [D_f L_f + D_o (S_f - L_f)] \tag{67}$$

$$C_{\tau e} = \frac{1}{D_e S_f} \left[\frac{C_{\tau n}}{4} (D_f^2 - D_o^2) + C_{dt} D_f L_f + C_{dt} D_o (S_f - L_f) \right] \tag{68}$$

The mass of each float, m_f , can be obtained by using the following expression in Equation (69), where ρ_f denotes the density of the float:

$$m_f = v_f \rho_f + m_l \tag{69}$$

The numerical model considers the entire hose-string in deriving the mass per unit length, m , for a line having floats by using the float distribution through the line and the corresponding value of the type of base line having mass, m_l :

$$m = m_l + \frac{m_f}{S_f} \tag{70}$$

The volume of a single float, v_f , can be calculated using the following equation:

$$v_f = \frac{\pi}{4} (D_f^2 - D_o^2) \cdot L_f \tag{71}$$

The volume per unit length of the hoseline with floats, v_{lf} , is obtained using the following equation:

$$v_{lf} = \frac{\pi}{4} D_{ol}^2 + \frac{v_f}{S_f} \tag{72}$$

3.5. Analysis Method

The methodology applied in this numerical modeling is based on the utilization of commercial software tools for offshore ocean modeling and some semi-empirical calculations, as well as comparative sensitivity studies. The methodology for the analysis in this research is conducted in stages, as presented in Figure 9. The first set of studies were on the buoy analysis-mesh convergence, hydrostatics and hydrodynamics. Next is the buoy motion study for the 6DoFs. It was used to obtain the motion characteristics of the motion RAOs, added mass, radiation damping, first-order wave exciting forces and second-order drift forces. It was then followed by the hose analysis for the sensitivity studies. After that, a comparative study on the coupled modeling of ANSYS AQWA and Orcina’s Orcaflex 11.0f was conducted. The study also involved both static and dynamic analysis in the method for the analysis. It was performed by carrying out the hydrodynamic analysis of the floating buoy using ANSYS AQWA R1 2021. The amplitude values for the motion called

motion RAOs are then loaded into Orcaflex 11.0f. The results of the numerical investigation and the sensitivity analysis are presented in Section 4.

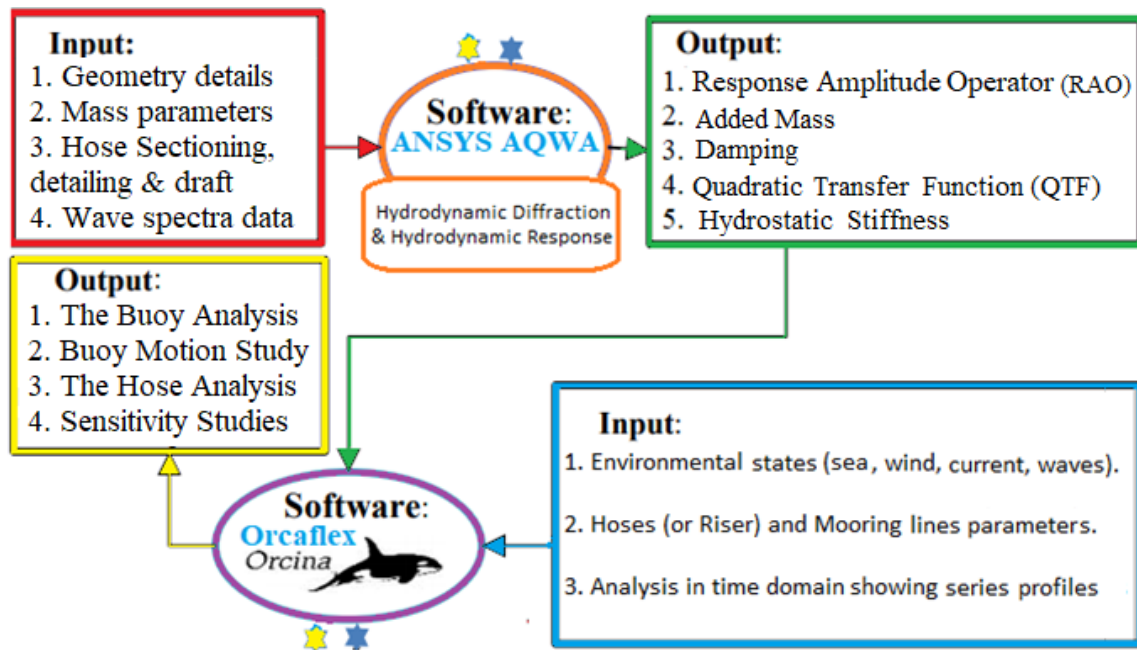


Figure 9. The methodology for the sensitivity studies in the numerical modeling.

3.6. Hose Load Cases

For the investigation, the full time for fully developed sea of 10,800 s (3 h) in real time was used for each simulation run in the Orcaflex analysis, with early hose disconnect also considered, as seen in the higher curvature results for extreme cases. For the hose analysis, the numerical investigation is conducted using the mooring load cases in Table 6. Based on global loadings, operational conditions were first considered. In this study, the submarine hoses are connected to the CALM buoy, and the six (6) mooring lines are utilized to moor the CALM buoy to the seafloor, as shown in Figure 5. The research aim focuses on two conditions—operating and survival. The complete operation conditions-loading and offloading cases are not included in this study. Figure 10 is an illustrative description for the mooring conditions with the load cases applied in the hose analysis, showing (a) damaged mooring line 01, (b) damaged mooring line 06 and (c) intact mooring lines. The operation case considered is the third case, whereby the moorings are intact and in a healthy condition. The whole operation, including the connection of the oil tanker to the CALM buoy and the hawser lines, is not considered in this study, as the study is limited to buoy motion and submarine hoses. The worst-case scenario for harsh conditions is calculated using the buoy offsets, mooring configuration and key environmental heading. For both wind and current, the 100-year extreme wind condition is taken into account. The combination of the wind, current and wave conditions are shown in Figure 10.

Table 6. Load case for hose analysis.

Condition	Mooring	Tanker	Heading	Configuration
Operation	Damage	Yes	In-line	Lazy-S Chinese-lantern
		Yes	In between or Cross	
	Intact	Yes	In-line	
		Yes	In between or Cross	

Table 6. Cont.

Condition	Mooring	Tanker	Heading	Configuration
Survival	Damage	Yes	In-line	Lazy-S Chinese-lantern
		Yes	In between or Cross	
	Intact	Yes	In-line	
		Yes	In between or Cross	
Extreme	Damage	No	In-line	Lazy-S Chinese-lantern
		No	In between or Cross	
	Intact	No	In-line	
		No	In between or Cross	

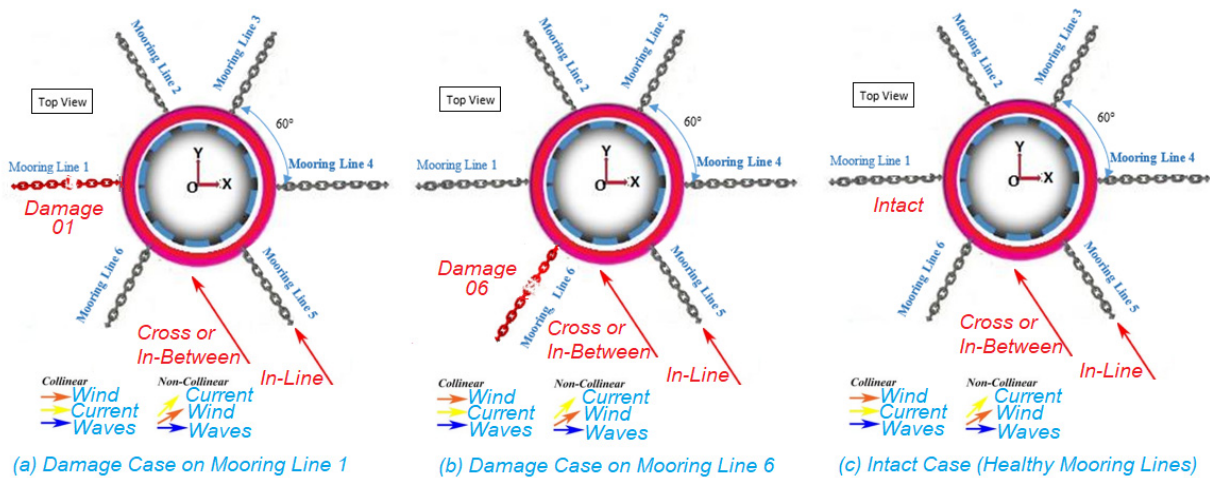


Figure 10. The description of the mooring conditions for the load cases applied in the hose analysis, showing (a) damaged mooring line 1, (b) damaged mooring line 6 and (c) intact mooring.

3.7. FEM Modeling

The Finite Element Model (FEM) for the CALM buoy hose system was designed in an ocean environment. Irregular waves under fully developed sea were utilized. The design of the hoses is based on simple beam theory, and later using Orcaflex line theory in Orcaflex version 11.0f [127–129]. Orcaflex applies line theory considers line elements and lumped mass at each section nodes, as shown in Figure 11a–c. For submarine hoses, the element type that it also applied is lines. Basically, this type of element is flexible with permissions for force displacements in bending, torsion and tension. Details on the principle of line theory used in the FEM of the submarine hose lines and the mooring lines are presented in [127–129]. Table 7 presents the details for the ocean. The system was tensioned using a mooring configuration consisting of six (6) moorings. It was then affixed to the anchor and attached to the body of the buoy skirt. Catenary equations were used to compute the statics of the mooring lines and the submarine hoses (see Section 3.11). The finite element model for the CALM buoy model, as depicted in Figure 12a,b, shows different components in Orcaflex.

Table 7. Parameters for the ocean and seabed.

Item	Value	Unit
Ocean Temperature	10	°C
Ocean Kinematic Viscosity of Ocean	1.35×10^{-6}	$m^2 s^{-1}$
Density of Water	1025	$Kg m^{-3}$
Wave Amplitude	0.145	m
Seabed Stiffness	7.5	$kN m^{-1} m^2$

Table 7. Cont.

Item	Value	Unit
Seabed Shape Direction	0	°
Water Depth	26.0 m (Chinese-lantern) and 100.0 m (Lazy-S)	m
Seabed Friction Coefficient	0.5	-
Seabed Model Type	Elastic Linear and Rigid Nonlinear Soil Models	-

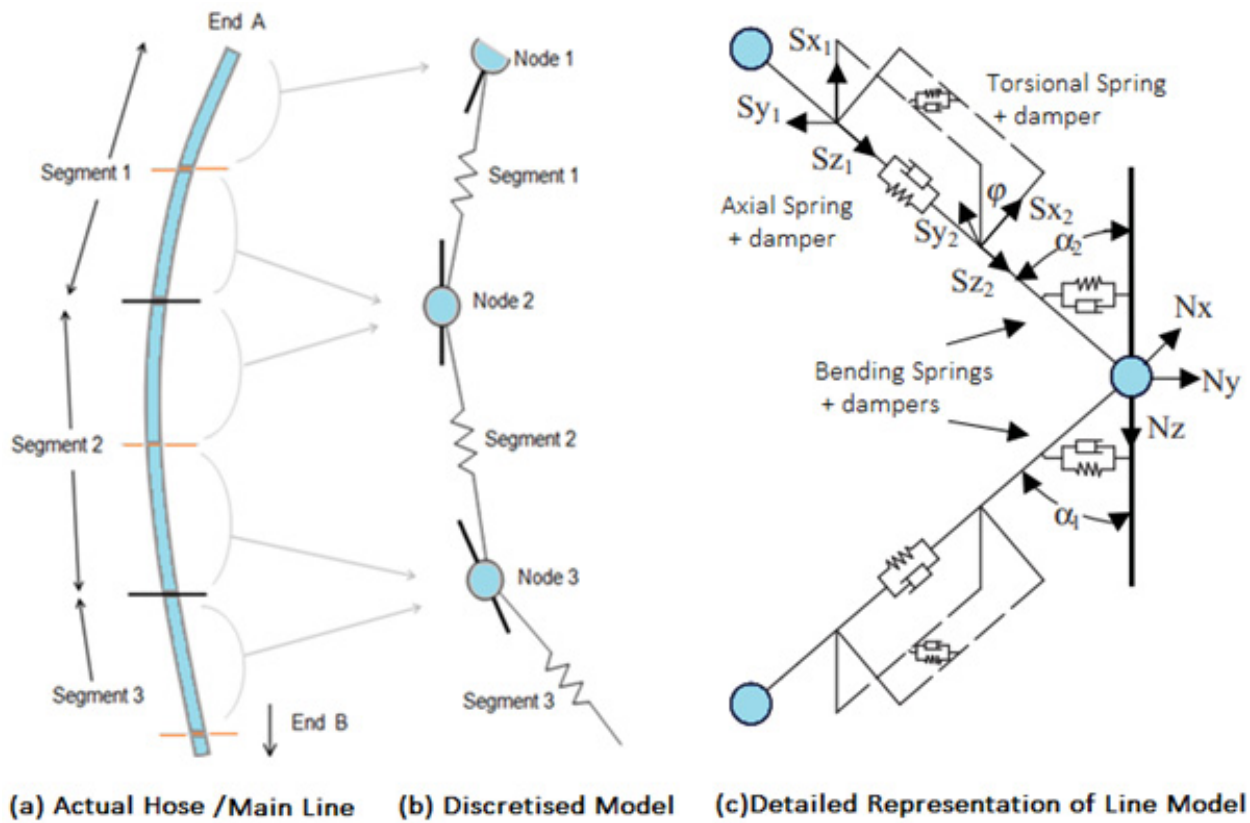


Figure 11. The Orcaflex line theory depicting (Adapted, courtesy of Orcina; Source: [127,128]).

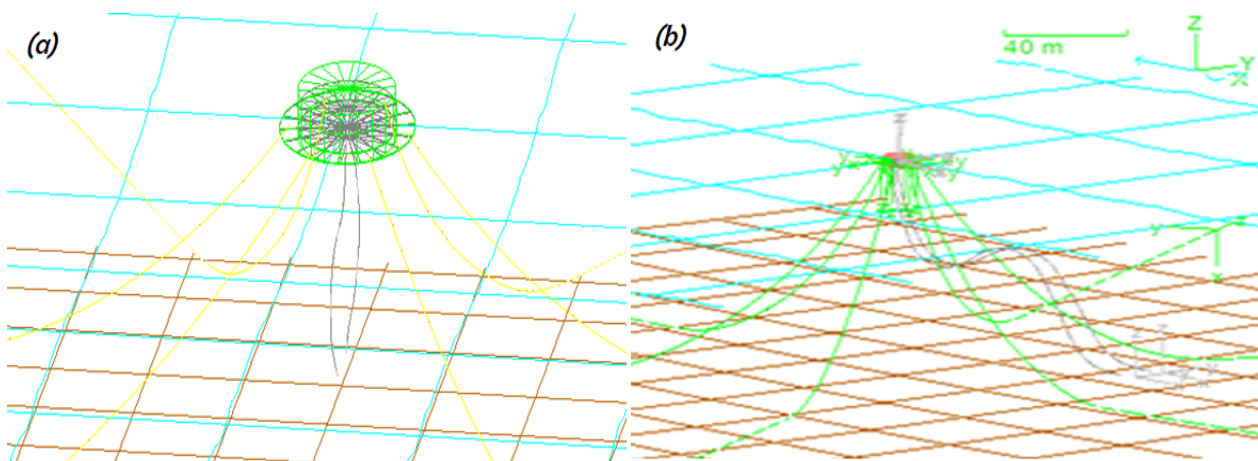


Figure 12. CALM buoy finite element model of (a) Chinese-lantern and (b) Lazy-S configurations.

3.8. Environmental Conditions

The modeling for the floating buoy is for operation in an ocean environment. The buoy is acted upon by some loadings, including waves, currents and other hydrodynamic forces. It was modeled according to recommendations of industry standards [132–135]. The environmental conditions for the three sea states considered for the global loading and this analysis are presented in Table 8. Figure 13 shows the JONSWAP (Joint North Sea Wave Project) wave spectrum for the (a) first sea state and (b) third sea state considered in this investigation. It shows that the input wave conditions with different wave periods have different peak frequencies. The wave heading with a description of the wave angles is presented in Figure 14. For the load estimation, a uniform current profile was considered, and wind loads were added to the CALM buoy model. The current speed employed was 0.5 m/s, while the wind speed was 22 m/s, respectively. The current profile for the surface current and seabed current in the X-Y axes is detailed in Table 9. The wave spectra adopted for the investigation is the JONSWAP spectrum. This spectrum accounts for any imbalance in the energy flow within the wave system. Equation (73) is the JONSWAP spectrum [136–140], where ω is the angular frequency, ω_p denotes the peak angular frequency, g denotes gravitational constant for gravity, η denotes the incident wave amplitude and σ denotes the peak enhancement factor, while the other parameters σ , σ_1 and σ_2 are the spectral width parameters. These are also dependent on the significant wave height, H_s , and the zero-crossing period, T_z . According to findings in literature [127–129,140], using Equations (73)–(77), $\sigma_1 = 0.07$ and $\sigma_2 = 0.09$ are constants for sigma:

$$S_{\eta}(\omega) = \frac{\alpha g^2}{\omega^5} \exp \left[-\frac{5}{4} \left(\frac{\omega_p^4}{\omega^4} \right) \right] \gamma^a \tag{73}$$

$$S_{\eta}(\omega) = \frac{\alpha g^2 \gamma^a}{\omega^5} \exp \left[\left(-\frac{5}{4} \frac{\omega_p^4}{\omega^4} \right) \right] \tag{74}$$

$$a = \exp \left[-\frac{1}{2\sigma^2} \left(\frac{\omega_p}{\omega} - 1 \right)^2 \right] \tag{75}$$

$$\sigma = \sigma_1 \text{ for } \omega_p \leq \omega \tag{76}$$

$$\sigma = \sigma_2 \text{ for } \omega_p > \omega \tag{77}$$

These are also dependent on the zero-crossing period, T_z , and the significant wave height, H_s . The JONSWAP spectrum is modified from the Pierson–Moskowitz spectrum [141], to take care of regions that have geographical boundaries so as to limit the fetch as regards the wave generation. With modifications made to the JONSWAP equation, better capturing was made in regions with geographical boundaries that had a limit on the fetch during the generation of waves.

Table 8. Wave parameters for the three load cases.

Case No.	H_s (m)	T_z (s)	T_p (s)	Conditions	Wave Angles (°)	Hydrodynamic Loads (HL)
01	1.87	4.40	5.50	Operation	0, 30, 60, 90, 120	Coupled (has HL), Uncoupled (no HL)
02	2.40	6.10	7.85	Extreme	0, 30, 60, 90, 120	Coupled (has HL), Uncoupled (no HL)
03	4.10	5.50	9.65	Survival	0, 30, 60, 90, 120	Coupled (has HL), Uncoupled (no HL)

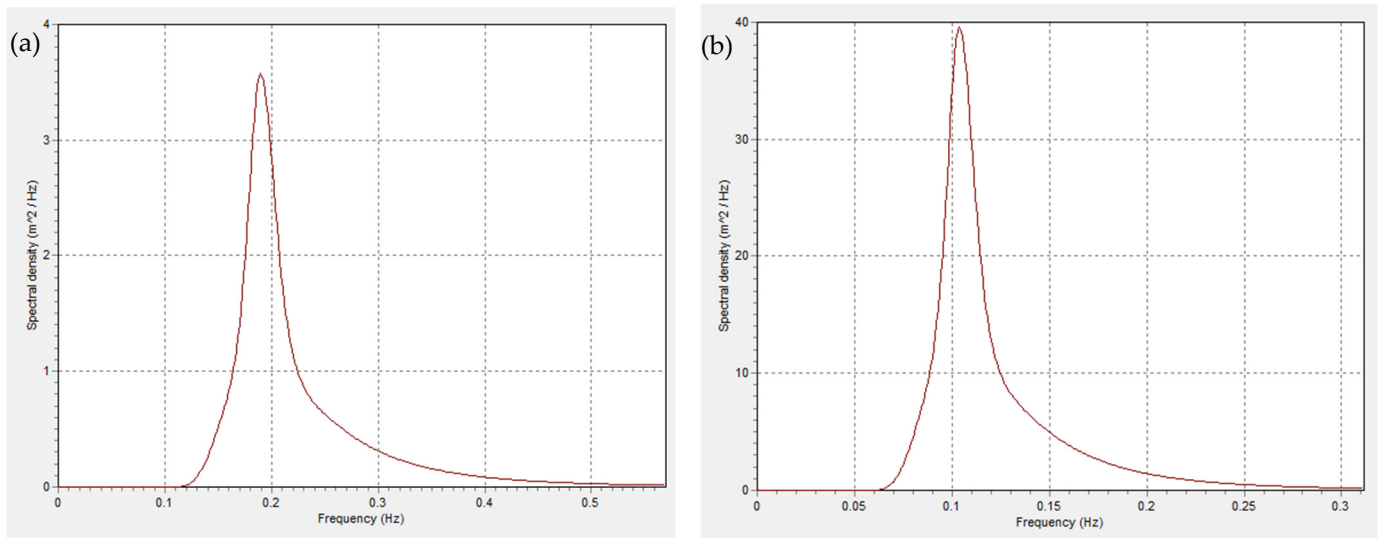


Figure 13. The JONSWAP wave spectrum for the (a) first sea state and (b) third sea state.

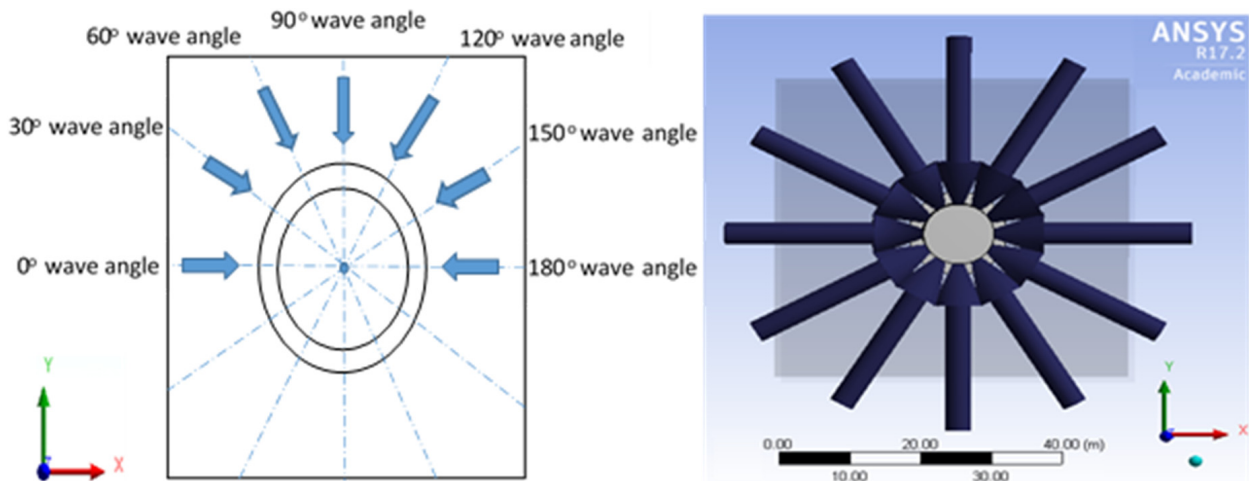


Figure 14. Definition of wave angles on the buoy at 30° intervals showing wave heading.

Table 9. Wind and current parameters.

Item	Value	Unit
Current Direction	180.00	°
Surface Current	0.50	ms ⁻¹
Seabed Current	0.45	ms ⁻¹
Wind Speed	22.00	ms ⁻¹
Wind Type	Constant	-
Density of Air	1.225	Kg m ⁻³
Kinematic Viscosity of Air	0.000015	m ² s ⁻¹

3.9. Buoy Hydrostatics

The details for the buoy hydrostatics are given in Table 10. The local cartesian coordinate system was considered in the numerical model. Since the floater behavior is represented by the RAOs with buoy hydrostatics, the motion characteristics from the RAOs generated were loaded into the Orcaflex model. The hydrostatic aspect of the numerical model was applied in the buoy for the coupled dynamic analysis using Orcaflex 11.0f. The AQWA hydrodynamics/panel model of the buoy was free, without any mooring line and hoses attached to it, as similarly applied in other offshore structures. Details of the

stiffness matrix for the buoy are presented in the literature [1]. In obtaining the RAOs, the mooring lines and hoses were not included in the ANSYS AQWA model. The models are validated in Section 3.11. Then, it was used in conducting sensitivity studies with the validated numerical model of the CALM buoy hose system. Figure 15 depicts the model ocean view of the CALM buoy in free-floating mode for hydrodynamic and hydrostatic analysis. The dimension for the sea model box is 150 m × 150 m, as the box illustrates the X and Y directions of the sea conducted under fully developed sea conditions.

Table 10. Parameters for the buoy hydrostatics.

Item	Value	Unit
Buoy Area	438.49	m ²
Buoy Volume	344.98	m ³
I _{xx} (Moment of Inertia)	433,137,937	kg m ²
I _{yy} (Moment of Inertia)	448,667,411	kg m ²
I _{zz} (Moment of Inertia)	433,137,937	kg m ²
CoG (Centre of Gravity)	−2.20	m
B _f (Buoyancy Force)	196,750,000	N

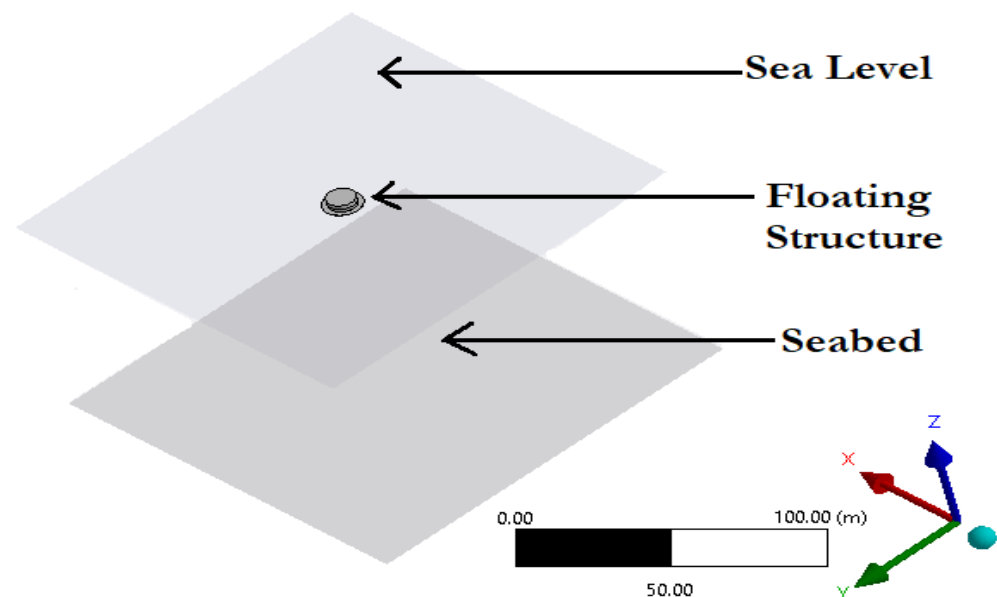


Figure 15. Model ocean view of the free-floating CALM buoy in ANSYS AQWA R1 2021.

3.10. Mesh Convergence

An extensive mesh convergence analysis in the diffraction study in ANSYS AQWA R1 2021 was conducted to validate the numerical model. A value of tolerance considered is 0.01 m and the highest element size considered was 1.25 m. In order to confirm that the study was conducted using the best effective element size in meshing, the range of the elements selected were from 1.25 m to 0.225 m. The mesh study was investigated by utilizing the panel model. This was conducted on the CALM buoy under ocean environment to study the tension, surge displacement and bending in the surge motion. The RAO values were obtained from the hydrostatic parameters, such as potential damping and added mass. For the convergence study in Figure 16, a single wave angle 0° was considered. Table 11 shows the results obtained from the effect of the maximum surge RAO that acts along the 0° incidences. From the statistical analysis, the maximum RAO variance and maximum RAO deviation were taken from 0.225 m mesh size. The study showed very small deviations in the RAOs obtained from the maximum at 0.25 m element size. Surge RAO is dimensionless, with the unit being m/m, as seen in the convergence plot. Precisely,

it is much less minimal, and much less than 3%, as observed in Table 11, which implies that the tolerated deviation considered in this analysis will save computational resources and also be sufficient and acceptable, validating this study.

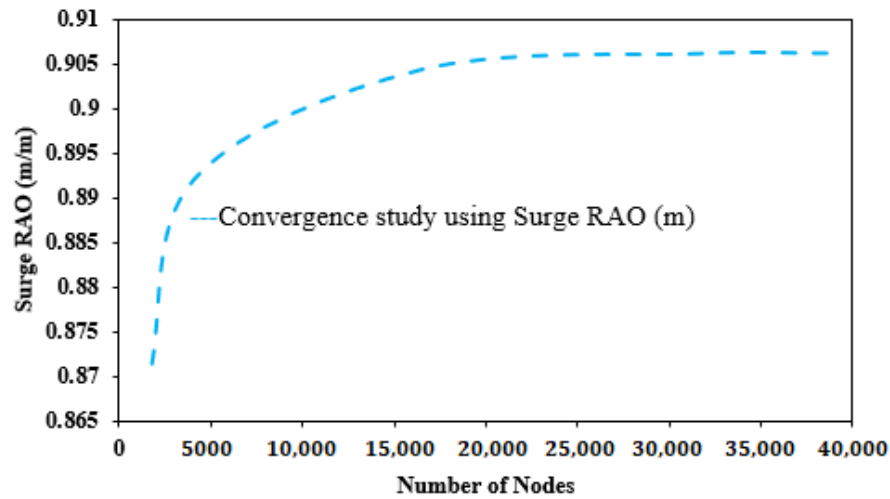


Figure 16. Convergence study on buoy using surge RAO (m).

Table 11. Convergence study using surge RAO.

Mesh Size	Nodes	Elements	Surge RAO (m/m)	Max. RAO Variance from 0.225 m	Max. RAO Deviation from 0.225 m
0.225	38,572	38,570	0.90610	0.000000	0.00000%
0.25	31,554	31,552	0.90605	0.000000	0.00004%
0.35	16,464	16,462	0.90427	0.000016	0.00126%
0.75	4070	4068	0.89206	0.000075	0.00863%
1.25	1628	1626	0.87012	0.000241	0.01551%

3.11. Model Validation

The validity of this model was carried out by a comparison of theoretical and numerical computations on the marine hose models. The catenary method was utilized in the statics calculation for computing the submarine hose and that of the mooring lines. An illustration of the catenary line with the global coordinate system in X-Z plane is given in Figure 17. Using the notations on the sketch in Figure 17, the catenary equation is considered as expressed in Equation (78), where H is the horizontal tension component of the system, w is the weight per unit length, z is the catenary line parameter for the distance from the seabed to the top of the line and x is the section length:

$$z = \frac{T_H}{w_s} \left[\cosh\left(\frac{xw_s}{T_H}\right) - 1 \right] \tag{78}$$

To obtain the curvature at sagbend, the tension components are required. The shape of the catenary can be obtained by calculation [60], using the expression in Equation (73). However, to compute the maximum curvature of the hoseline or mooring line at touch down point (TDP), Equation (79) can be applied:

$$\frac{1}{R} = \frac{w_s}{T_H} \tag{79}$$

where w_s is the submerged weight per unit length of hose-string or mooring line, x is the section length from TDP, T_h is the horizontal force acting at the seabed and z is the height

above seabed. Note that h and z can be used to depict vertical heights for the top section and TDP, respectively. In this case, z is considered for uniformity.

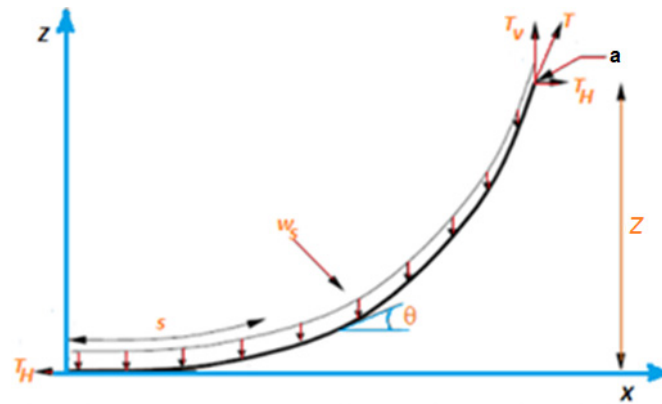


Figure 17. Forces on the catenary design of a mooring line.

To obtain the vertical force, T_v , and the horizontal force, T_H , acting at the topmost hose-end, the expressions given in Equations (80) and (81) are the relationships for T_H and T_v obtained theoretically as the centenary equations [60,142–145], where s denotes the hose arc-length, θ denotes angle along the horizontal plane, w_s denotes the submerged weight and z denotes the height above the seabed:

$$T_H = \frac{z \cdot w_s}{(\tan \theta)^2} \cdot (1 + \sqrt{[1 + (\tan \theta)^2]}) \tag{80}$$

$$T_v = s \cdot w_s \tag{81}$$

The arclength for the hose top tension, s_{top} , and the arclength at the hose TDP (touch down point) tension, s_{TDP} , which relate to the arclengths in the horizontal and vertical components, can be obtained using Equations (82) and (83), respectively:

$$s_{top} = h \cdot \sqrt{1 + 2 \cdot \frac{T_H}{h \cdot w_s}} \tag{82}$$

$$s_{TDP} = z \cdot \sqrt{1 + 2 \cdot \frac{T_H}{h \cdot w_s}} \tag{83}$$

The angle between the hoseline or mooring line and the x - y plane is given by:

$$\tan \theta = \frac{T_H}{T_v} \tag{84}$$

For the second validation regarding the coupling of ANSYS AQWA + Orcaflex approach, the validation part is certainly important. Since the present paper does not report on the experimental results, this validation needs to be included in the present study. Comparisons between analytical and numerical results are acceptable with more perspectives considered. In an earlier study [146], validations of marine hoses were conducted using the maximum tensions in horizontal and vertical components. In the present study, bending moments and stress deformations are used, as these generally reflect structural stiffness, for instance, pipeline deformation along the arc length during S-laying, although forces can be directly correlated to the deformations. In the present study, the results of the comparative study between the coupled model and the uncoupled model for two submarine hoses (Hose1 and Hose2) under 0° flow angle is presented in Figure 18. As observed in the comparisons in Figure 18, the first model case represents the uncoupled model, while the second model case represents the coupled model. The global loadings considered are the environmental data presented in Section 3.8. Comparisons were made between both

models in the validation study via numerical and statistical investigation. The result of the validation study and the computation is given in Table 12. It was recorded that the bending moment from the coupled model is 2.78 times greater than the uncoupled model. For each case of the coupled model, there were additional hydrodynamic RAO loads, which induced more responses in the bending moment and hose curvature. The uncoupled model has a lower bending moment and the average ratio from the statistical average ratio computed was found to be 0.53% for the bending moment component. From the comparisons on both component forces, it can be observed that both parameters considered agreed well, and thus, the study is validated.

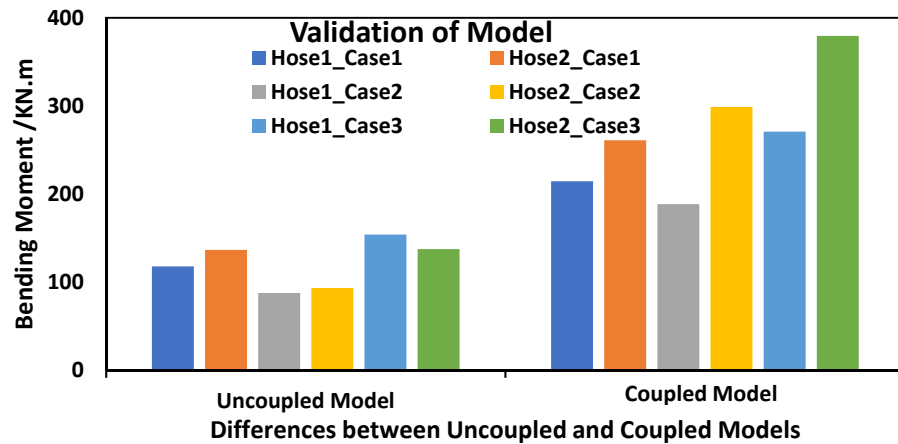


Figure 18. Validation study using the bending moment of the submarine hose, comparing the uncoupled and coupled models.

Table 12. Validation study using the bending moment of the submarine hose.

Parameters	Bending Moment (KN.m)		Average Ratio (Uncoupled/Coupled)
	Uncoupled Model	Coupled Model	
Hose1_Case1	117.6735	214.4112	0.54882161
Hose2_Case1	136.5212	261.0225	0.523024643
Hose1_Case2	87.54206	188.5113	0.464386273
Hose2_Case2	93.11749	298.8106	0.311627131
Hose1_Case3	153.9478	270.7054	0.568691278
Hose2_Case3	137.3706	379.3597	0.362111737
Total	726.17265	1612.8207	2.778662673

The third validation is based on the application by considering some models studied on existing theoretical marine hose models [96–100] and experimental hose models [147–150]. These models were compared to that of this present study and showed effective similarities in hose behavior. In addition, an application of existing Orcaflex marine pipeline models on marine hoses validated using tension were conducted using the Chinese-lantern configuration [146] and catenary S-lay marine pipes conducted with full scale ocean tests [151]. Furthermore, deeper mechanism analysis was carried in addition to the current discussion, mainly focusing on the influence of certain parameters on the structural response. This includes studies on the shape effect, the methods for optimizing the designs from the results obtained and using effective design suggestions. The consideration for the validation includes the key parameters investigated on the marine hoses, and the bending moment was selected. These considerations were conducted to confirm the model’s validity.

3.12. Dynamic Amplification Factor (DAF)

The comparison on computations led to the additional investigation on the response behavior based on design factors and guidance values that could be generated from this

study. Parametric studies conducted on the hoses included the bending moment, effective tension and hose curvature. *DAF* investigations were also performed on these hose parameters investigated. The dynamic amplitude factor or dynamic amplification factor (*DAF*) is depicted simply as the response factor for the dynamic response amplitude versus the static response amplitude. In that respect, the relationship for the Dynamic Amplification Factor of hose (DAF_{hose}) is given in Equation (85). The static response amplitude is the response amplitude operator obtained during static analysis. More fundamental studies on *DAF* are available in the literature [152,153].

$$DAF_{Hose} = \frac{\text{Dynamic Response Amplitude (coupled hose model having hydrodynamic loads)}}{\text{Static Response Amplitude (uncoupled hose model lacking hydrodynamic loads)}} \quad (85)$$

In real environmental ocean conditions, accurate prediction of the amplitude motion of the offshore structure must be performed before any offshore operation is carried out, as specified in design guidelines. This first design analysis is conducted initially in the static stage. Based on the *DAF* studies carried out, some *DAF* values were recommended for the submarine hoses; however, these are relative to the submarine hose position on the seabed.

4. Results and Discussion

In this section, the results from the numerical studies on the motion response of the CALM buoy are presented. The results from the sensitivity studies includes some parametric studies obtained from the numerical studies. The influence of hydrodynamic loads on CALM buoy submarine hoses has been observed to have an influence on the hose-string curvature, effective tension and the bending moment.

4.1. Results of Hydrodynamic Studies

The results of the hydrodynamic studies are presented in this section.

4.1.1. Results of the Coupled and Uncoupled Models

The coupled and the uncoupled models are studied in this section. The bending moment profile showing Hose1, Hose2, three sea states and five wave angles utilized in the uncoupled model is shown in Figure 19, while that for the coupled model is shown in Figure 20. From Figure 19, it can be observed that different wave angles reflect a different profile on the bending moment without added RAO wave loads; however, they are closely related. The 0° wave angle has the highest profile among the five cases in this study. It shows that at 0° incidences, the bending moment per hose case is higher than that of 30°, 60°, 90° and 120° incidences. Additionally, the Hose1_Case2 and Hose2_Case2 have the highest distribution of 153.95 kN and 137.37 kN, respectively. This implies that the extreme environmental loadings have a direct impact on the hydrodynamic characteristics of the submarine hoses. It can also be seen that the minimum values for each hose case occurred at 90° in Case1 and Case2 but not in Case3. This implies that based on the earlier cases, the hose characteristics is induced at higher environmental loadings. Also, the hose wave incidence at right angles will induce higher diffraction on the hose. Thus, there is a higher response due to the shape of the hose and the wave–current interaction that it undergoes at that time period. This implies that there are highly sensitive responses from higher time periods by the hoses. In Figure 20, it was recorded that the coupled model (having the addition of hydrodynamic RAO wave loads) had higher distributions compared to the uncoupled model (without addition of hydrodynamic wave loads) in Figure 19. The results in Figure 20 shows that at 0° incidences, the bending moment per hose case is higher than that of 30°, 60°, 90° and 120° incidences. Additionally, the Hose1_Case2 and Hose2_Case2 have the highest distribution of 270.71 kN and 379.36 kN, respectively. Next to the 0° cases are the 30° cases, which showed a closer profile relationship to the 0° cases. However, it can be observed that the hose bending moments at Case3 in Hose1_Case3 for 30° (360.01 kN) is higher than the hose bending moments at Case3 in Hose1_Case3 for 0° (270.71 kN). This implies that the higher time period also has an effect on the hose at that

wave angle. A similar higher profile is observed in 120°, which is about a quadrat turn through of 30° incidence. The comparison between the uncoupled and the coupled models in Figures 19 and 20, respectively, shows that the coupled models generally have higher bending moment than the uncoupled models.

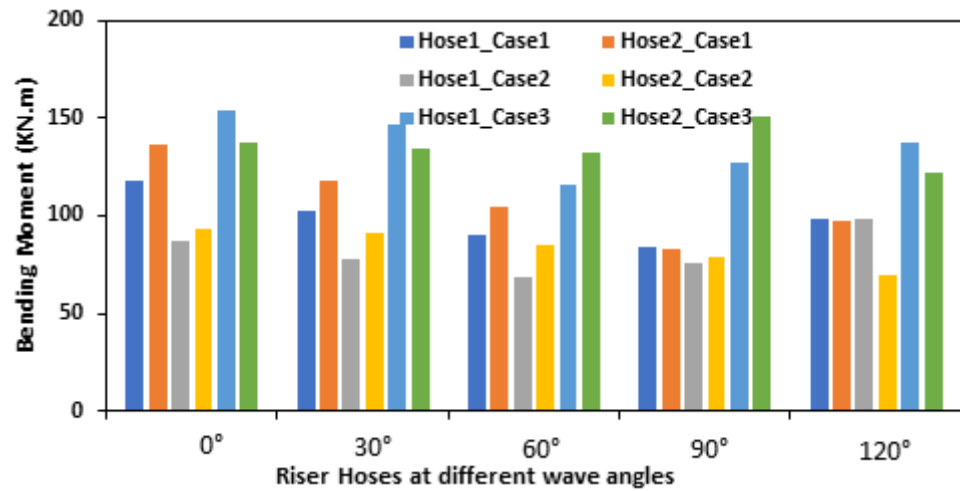


Figure 19. Bending moment profile for uncoupled model showing Hose1, Hose2, three sea states and five wave angles.

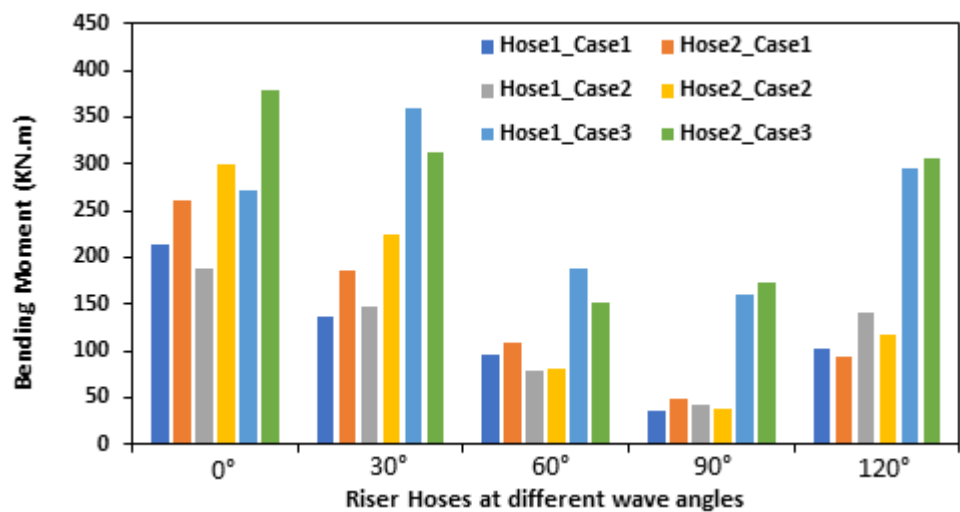


Figure 20. Bending moment profile for coupled model showing Hose1, Hose2, three sea states and five wave angles.

4.1.2. Results of the Hose Curvature Sensitivity

The curvature profiles for the marine hose under Lazy-S and Chinese-lantern configurations showing the cases including loadings from hydrodynamics and excluding loadings from hydrodynamics are, respectively, presented in Figure 21a–d. A number of deformations were observed in the hose occurs where the MBR is high. Similarly, a number of curvature distributions are observed from the behavior of the submarine hoses via dynamic analysis. As observed in the Figure 21a–d, the 0° flow angle models have the highest curvature via arc length of the hose in both configurations. However, the 90° flow angle models reflected minimal curvature via the arc length of the hose. Damping is one method to minimize hose curvatures, in addition to the inclusion of the hydrodynamic loads. It was also observed that the hoses subjected to cross-flow directions in the cases for 0° in both Lazy-S and Chinese-lantern configurations presented greater curvatures, which further developed on inclusion of the hydrodynamic loads. While the curvature plot in

the Lazy-S configuration cases sag, cases are hugging in the Chinese-lantern configuration. Additionally, the curvature profiles for the Lazy-S configurations have higher curvatures at the top connections, which can be attributed to the weight from the longer length of the hose-string at its connection point to the manifold on the CALM buoy.

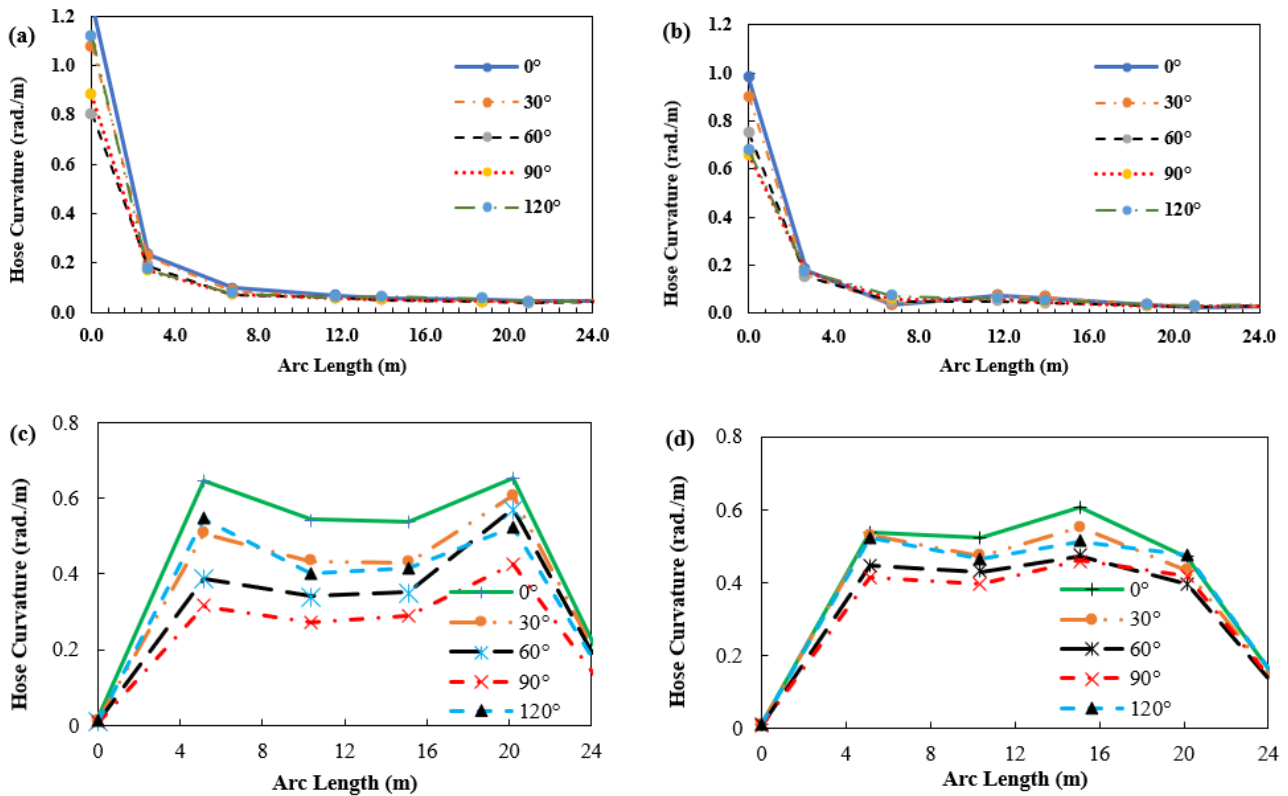


Figure 21. Influence of loadings from hydrodynamics on the curvature of the submarine hose. (a) Hose Curvature including hose hydrodynamic load in Lazy-S config. (b) Hose Curvature excluding hose hydrodynamic load in Lazy-S config. (c) Hose Curvature including hose hydrodynamic load in Chinese-lantern config. (d) Hose Curvature excluding hose hydrodynamic load in Chinese-lantern config.

4.1.3. Results of the Hose Effective Tension Sensitivity

The effective tension profiles for the marine hose under Lazy-S and Chinese-lantern configurations showing the cases, including the loadings from hydrodynamics and excluding the loadings from hydrodynamics, are, respectively, presented in Figure 22a–d. The tension profiles present a steady distribution running through the arc length of the hoses. However, the comparative studies on both configurations shows that there are higher distributions recorded in the Lazy-S case than the Chinese-lantern case, but the Chinese-lantern case has more fluctuations than the Lazy-S case. This is attributed to the result from bending in response to waves and currents. The distribution recorded on the effective tension profile is not undulating or fluctuating like that of the bending moment profiles presented in Figure 23. The reason is that hose tensions are not always a function of the flexural stiffness, but due to nonlinearities in the hose material properties. It was also observed that the cross-flow model cases, in particular 0°, exhibited greater tensions in comparison to 90°. Thus, it can be deduced that an increase in the effective tension can be induced by increasing the hydromantic loads of the hose. In addition, the points of attachment of the hoses to the PLEM and to the manifold underneath the CALM buoy both exhibited maximum effective tensions that were of high magnitudes. Thus, the angle of inclination of design for the manifold is recommended to be at about 30°, as this manifold angle enhanced better results, but it is also subject to the manufacturer’s choice, the en-

vironmental conditions and the marine hose properties. Lastly, the hose-string recorded highest flexural stiffness and highest axial stiffness that resulted from the end-restrictions, but other sections are relatively flexible. More flexible hose sections with fewer bending moments may be used to withstand hydrodynamic loadings, and the float type for the hoses used may require more inertia properties.

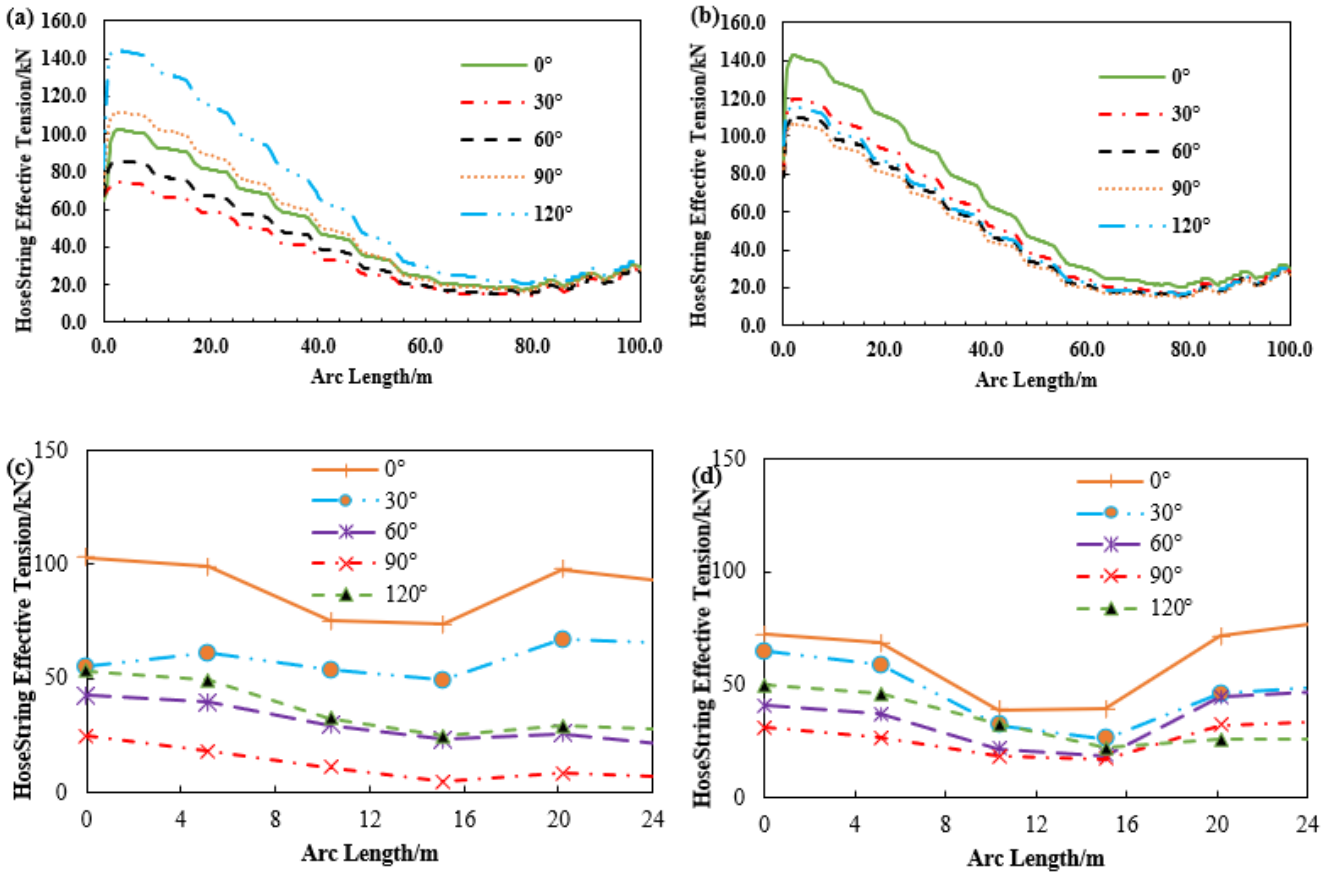


Figure 22. Influence of loadings from hydrodynamics on the effective tension of the submarine hose. (a) Coupled Hose Effective Tension in Lazy-S config. (b) Uncoupled Hose Effective Tension in Lazy-S config. (c) Coupled Hose Effective Tension in Chinese-lantern config. (d) Uncoupled Hose Effective Tension in Chinese-lantern config.

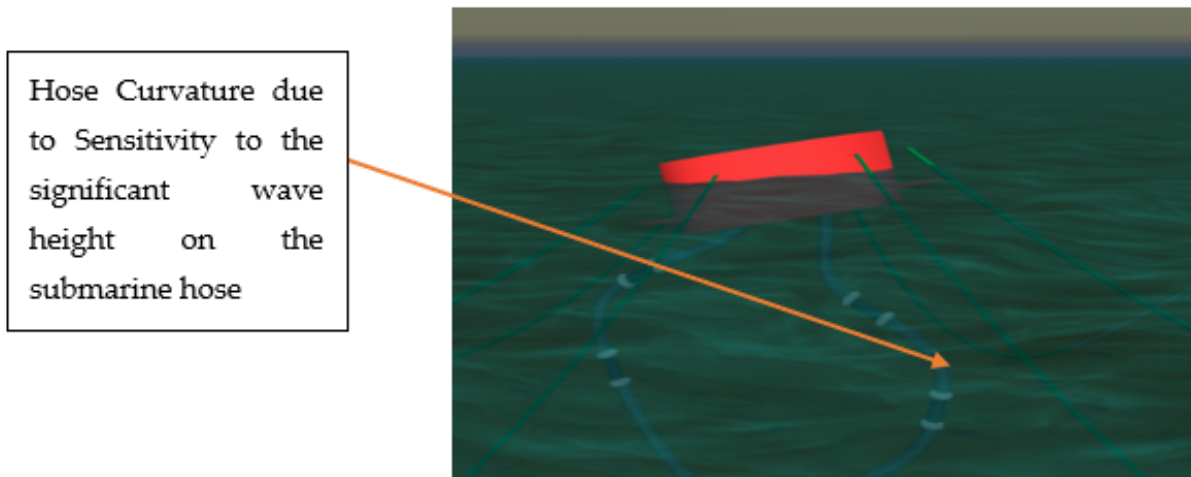


Figure 23. Curvature of submarine hose in Chinese-lantern configuration.

4.1.4. Results of Hose Bending Moment Sensitivity

The sensitivity of hose bending moment was also investigated in this research. As observed in Figure 23, the curvature of the hose from the bending moment is within the design limit, as stipulated in OCIMF [34]. Wave and current loads, as well as other hydrodynamic loads, induce the hose curvature. The bending moment profiles for the marine hose under Lazy-S and Chinese-lantern configurations showing the cases including the loadings from hydrodynamics and excluding the loadings from hydrodynamics are, respectively, presented in Figure 24a–d. As is evident in Figure 24c,d, there are significantly greater bending moments recorded at both ends of the marine hose. However, the bending moments for the arc length located within the middle and in between end sections have minimal bending moments recorded. The bending moment profiles recorded at the two ends of the marine hoses under the cases including the hose hydrodynamic loads. However, the hose sections that lie in between have significantly larger moments, with the exception of 90°. The bending moment behavior resulted from the twisting of the hose. From the comparative studies on Lazy-S and Chinese lantern cases, more undulations are observed in the lazy-S cases than the Chinese-lantern cases, which is due to the longer length of the submarine hoses, and the floats attached on the submarine hose-string in the Lazy-S configuration. During twisting, the hose deformations were observed to also be a function of the wave and the buoy rotations. Thus, larger moments from the twisting induced at 90° for the Lazy-S configuration is different from that of the Chinese-lantern configuration. In terms of energy dissipation, higher energy magnitudes are released during twisting than during bending. This, in turn, results in relatively lesser stiffness of the buoy on the system.

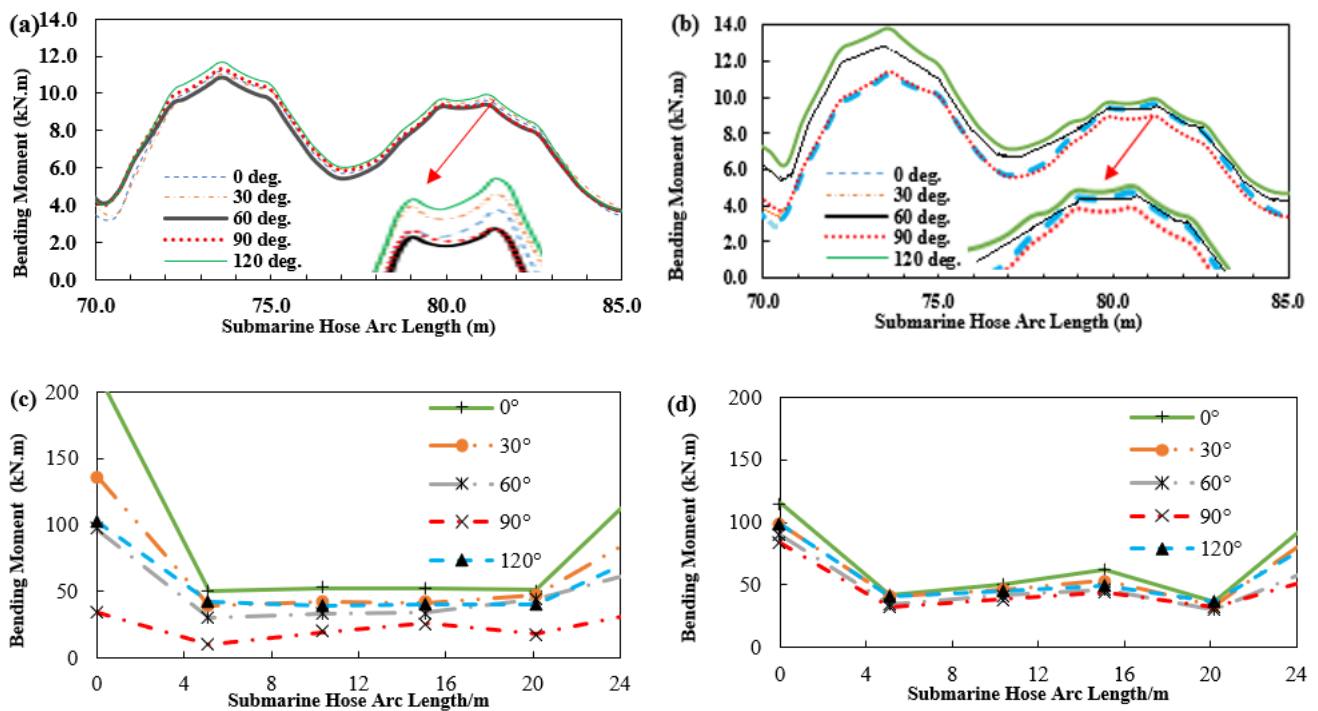


Figure 24. Influence of hydrodynamic loads on the bending moment of the submarine hose. (a) Coupled model for hose bending moment in Lazy-S config. (b) Uncoupled hose bending moment in Lazy-S config. (c) Coupled hose bending moment in Chinese-lantern config. (d) Uncoupled hose bending moment in Chinese-lantern config.

4.1.5. Results of DAF of hose (DAF_{hose}) Sensitivity

The sensitivity studies on the DAF_{Hose} for marine hoses are calculated by considering one submarine hose-string, Hose1, as presented in Figure 25a–f. The comparisons of the curvature profiles for Lazy-S and Chinese-lantern configurations showing the cases

including the hydrodynamic loads and excluding the hydrodynamic loads are shown in Figure 25a,b by the curvature DAF_{Hose} . The behavior of submarine hoses is subject to the buoyancy of the hose and the attached floats. However, with some flexibility in the hose-string under waves and current loadings, the hose-string is also designed to be resistant to such forces and moments, which can result to high curvatures. As a result of that, the floats are positioned at strategic positions; however, the locations having maximum bending require additional reinforcements. In the Lazy-S configuration in Figure 25a, high curvature profiles are observed in 0° , similar to the result obtained during accidental operation (disconnection), as that presents the most threatening scenario. However, the average hose curvature DAF_{Hose} is not that high. In the worst cases of hose disconnection, the DAF_{Hose} could have such high values of 2.5; however, the guidance value of 1.5–2.0 for curvature DAF_{Hose} is advised here, as seen Figure 25b in the normal operation with Chinese-lantern configuration. In Figure 25c,d, the profiles of effective tension DAF_{Hose} on the submarine arc length. According to the presented analyses, a guidance value of 1.0–2.0 is suggested for effective tension DAF_{Hose} and bending moment DAF_{Hose} . In offshore field practice, the determination of significant tensions is at the touch down zone (TDZ), and connection to PLEM and at the buoy manifold. This might be as a result of higher responses from the wave frequency motion, affected by damping, induced by the wave drift and perturbed by the seabed parameters. As such, the effective tension may be uniformly distributed along the hose arc length, but varying bending moments. This behavior is also due to the effect of the hydrodynamic coefficients of the buoyancy floats on the hose body. From the DAF curves, it can be observed that the connections had the highest bending moments. This can be attributed to some drag occurrence on the floating buoy. In principle, there is viscous drag resulting from friction between the surface of the buoy's body and the fluid particles. Thus, reducing both the coefficient of drag and the coefficient of damping is one method that is recommended to offset this phenomenon. Another method is to increase the reinforcement along such locations of high bending. The DAF_{Hose} for the bending moment distributions throughout the hose for Lazy-S and Chinese-lantern configurations showing the cases including hydrodynamic loads and excluding hydrodynamic loads arc length is presented in Figure 25e,f. In a similar fashion, the design recommendation for the bending moment DAF_{Hose} is a guidance value of 2.0. It is also recommended that accidental conditions are investigated in further studies based on hose disconnections, to predict the structural effect on the structure's integrity and ascertain safety guidelines for improving operations on CALM buoy-hose systems.

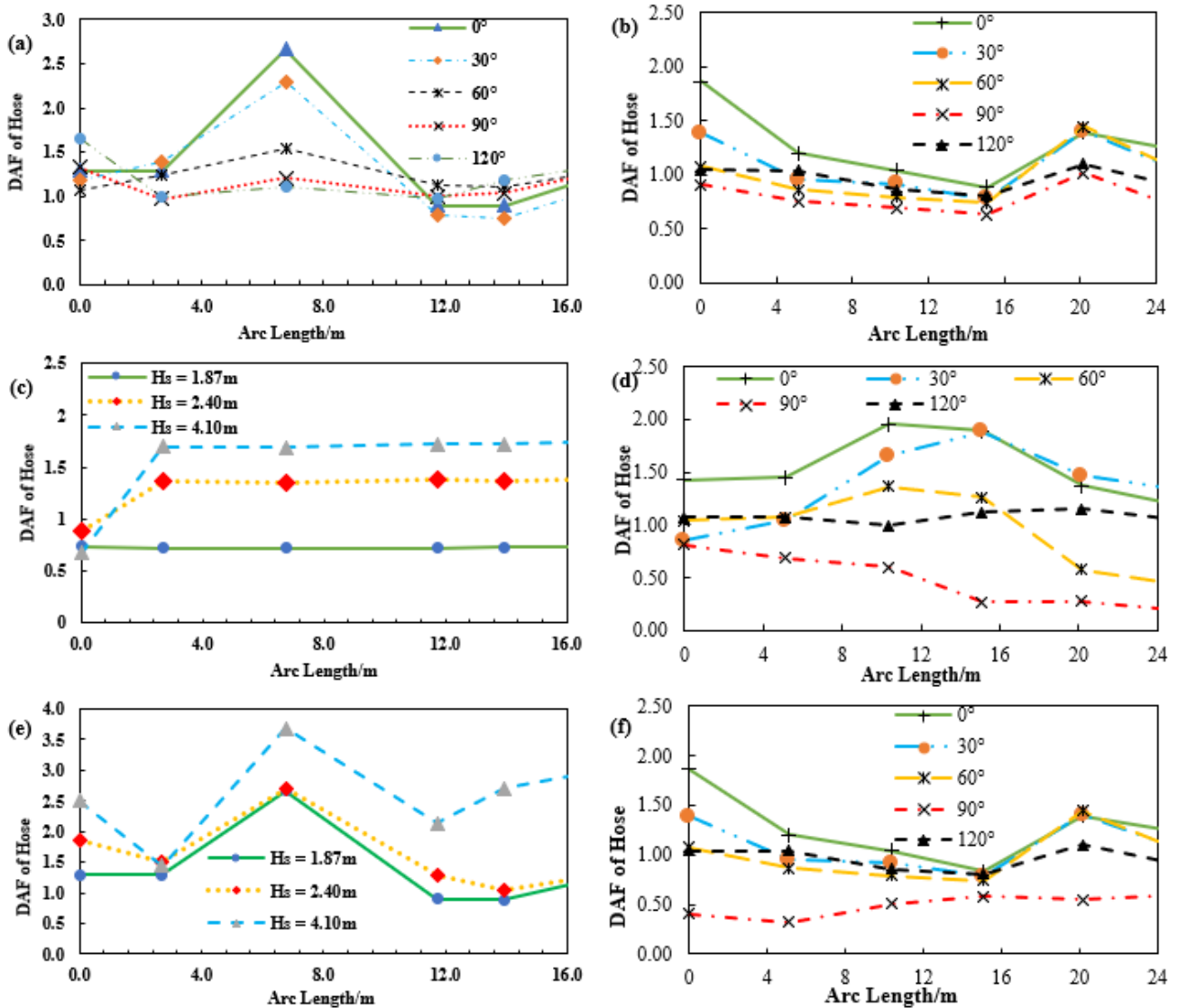


Figure 25. Influence of loadings from hydrodynamics on the DAF_{Hose} of the submarine hose. (a) Curvature DAF_{Hose} for the hose in Lazy-S config. (b) Curvature DAF_{Hose} for the hose in Chinese-lantern config. (c) Effective Tension DAF_{Hose} for the hose in Lasy-S config. (d) Effective Tension DAF_{Hose} for the hose in Chinese-lantern config. (e) Bending moment DAF_{Hose} for the hose in Lazy-S config. (f) Bending Moment DAF_{Hose} for the hose in Chinese-lantern config.

4.2. Results of the Wave–Current Interactions

The results of the wave–current interaction studies are presented in this section.

4.2.1. Results of the Current on Buoy Motion RAOs (Response Amplitude Operators)

The effect of the current velocity on the CALM buoy motion RAOs have been presented in this section. From the literature review, the effect of current velocity for the wave forces acting on the CALM buoy motion has not been presented in literature, but there are exciting works on other floating structures, such as semisubmersibles [55–58,154]. It should be noted that the CALM buoy has 6DoFs; however, the results of the surge, heave, pitch and yaw presented in Figure 26 are to show the influence of wave–current interaction and the effect of current velocity on the floating buoy. This investigation was conducted using three current profiles: 0.5 m/s, 1.0 m/s and 1.5 m/s. The RAOs were obtained under irregular waves using the environmental condition for extreme cases. It was recorded in Figure 26a that the higher the current velocity, the lower the surge profile. However, from

Figure 26b–d, it was recorded that the higher the current velocity, the higher the heave, pitch and yaw profiles. Furthermore, this confirms that variation in the current velocity affects the buoy under different motions by displaying unique response characteristics. Thus, recommendations include that CALM buoy hose systems should be practically well monitored using real-time monitoring systems, such as Offshore Monitoring Systems (OMS), Buoy Monitoring Systems (BMS) and Hose Monitoring Systems (HMS). Secondly, findings on the CALM buoy motion are with respect to the environmental conditions, and not representative of all sea conditions. However, the CALM buoys respond to both regular and irregular waves, as well as currents, depending on its collinearity.

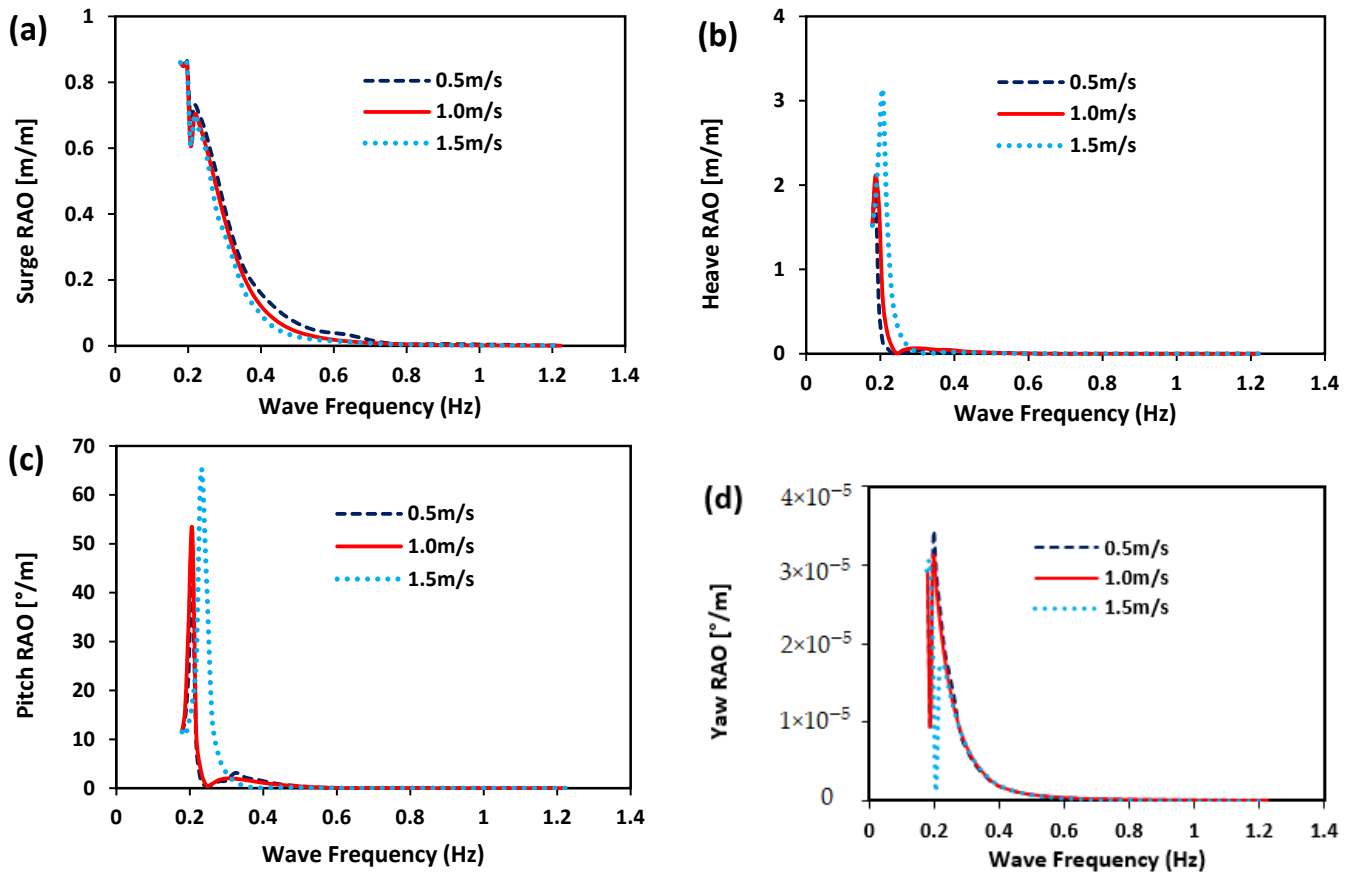


Figure 26. Influence of the current velocity on the motion RAOs for the CALM buoy, showing (a) surge, (b) heave, (c) pitch and (d) yaw.

4.2.2. Results of the Current on First-Order Wave Forces from CALM Buoy Motion

The effect of current velocity on the CALM buoy motion RAOs have been presented in this section. From Figure 27, it can be observed that the current has some effect on first-order wave forces for the different motions of the CALM buoy. This investigation was conducted using three current profiles: 0.5 m/s, 1.0 m/s and 1.5 m/s. The first-order wave forces were obtained under irregular waves using the environmental condition for extreme cases. It was recorded in Figure 27a that the higher the current velocity, the lower the surge profile. Contrary to this, in Figure 27b, the higher the current velocity, the higher the heave profile. In Figure 27c,d, the higher the current velocity, the lower the pitch profile and the lower the yaw profile, respectively. This shows that the current velocity has a direct relationship with the motion behavior. This makes some contribution to its hydrodynamic characteristics, but further research is required.

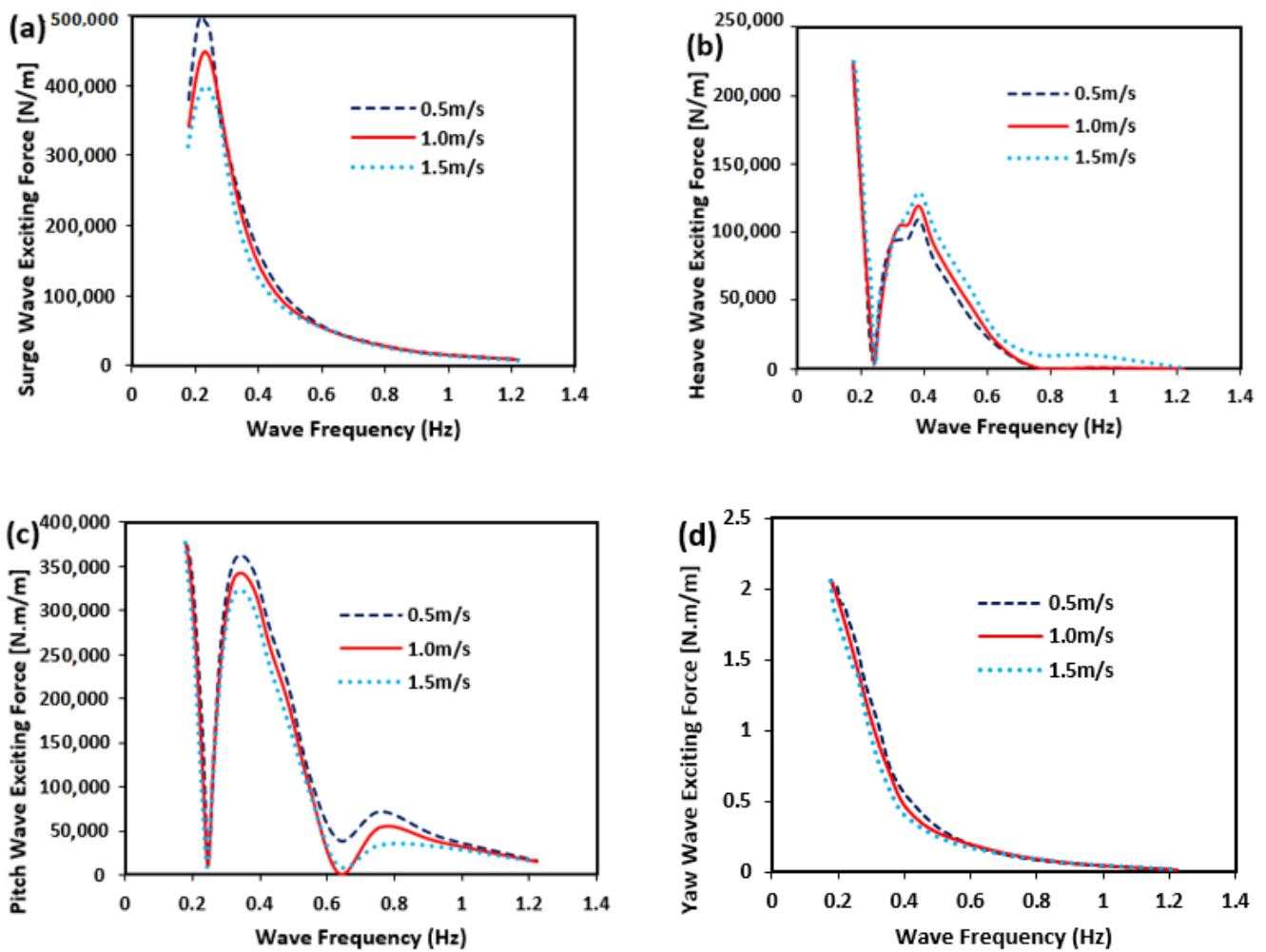


Figure 27. Influence of current velocity on the first-order forces for the CALM buoy, showing (a) surge, (b) heave, (c) pitch and (d) yaw.

The motion response is also a function of the ocean current, azimuthal direction, system acceleration, system velocity and the relative position of the attached hoses and mooring lines. The first-order wave forces on this system for the three different current velocities present similarities in form and profile. Additionally, they have different peaks on the surge, heave, pitch and yaw, but at the same natural frequency range for the system. The effect of the current velocity on the yaw motion is least or almost negligible, as observed in Figure 27d. However, due to the resonating frequency, the effect of the current velocity is relative to the motion—if translational, such as surge and heave, or rotational, such as pitch and yaw. In the case of the heave, the frequency profile is higher from 0.299 Hz to 1.223 Hz, unlike in the surge motion where the frequency profile is 0.179 Hz to 0.278 Hz. This behavior shows a relationship between first-order wave forces and the three current velocities investigated. However, further investigation is also recommended by considering the effect of CALM buoys with different draft sizes. Based on studies on Boundary Element Methods [155–158], waves and currents impact floating bodies. These earlier studies found that wave energy is absorbed, including elevated bodies and deformable bodies. Unlike the submarine hose, the CALM buoy is considered an elevated body that floats on the surface of the sea, across its draft line. This study also shows a variation in the effect of current velocity from different motion characteristics.

4.2.3. Results of the Seabed Current and Surface Current Sensitivity on Hose

The sensitivity of current was investigated for both the seabed current and surface current on the nonlinear seabed model in the Lazy-S configuration. The surface current velocity has a pertinent function in designing CALM buoy systems for loading and offloading operations. To investigate its influence, some surface current values are used: 0.45 m/s, 0.65 m/s, 0.75 m/s, 0.9 m/s and 1.0 m/s. As the surface current velocity increases, the bend radius (curvature) decreases, the bending moment decreases and the effective tension increases, as in Figure 28a,b. Considering the seabed currents, the seabed current velocity parameters considered are as follows: 0.35 m/s, 0.45 m/s, 0.75 m/s and 0.9 m/s. For the same surface current velocity, an increment on the seabed current velocity has corresponding reduced effective tension and reduced bending moment, as shown in Figure 28c,d. An increase in seabed current velocity gives a reduced bend radius (curvature) and an increased effective tension and bending moment.

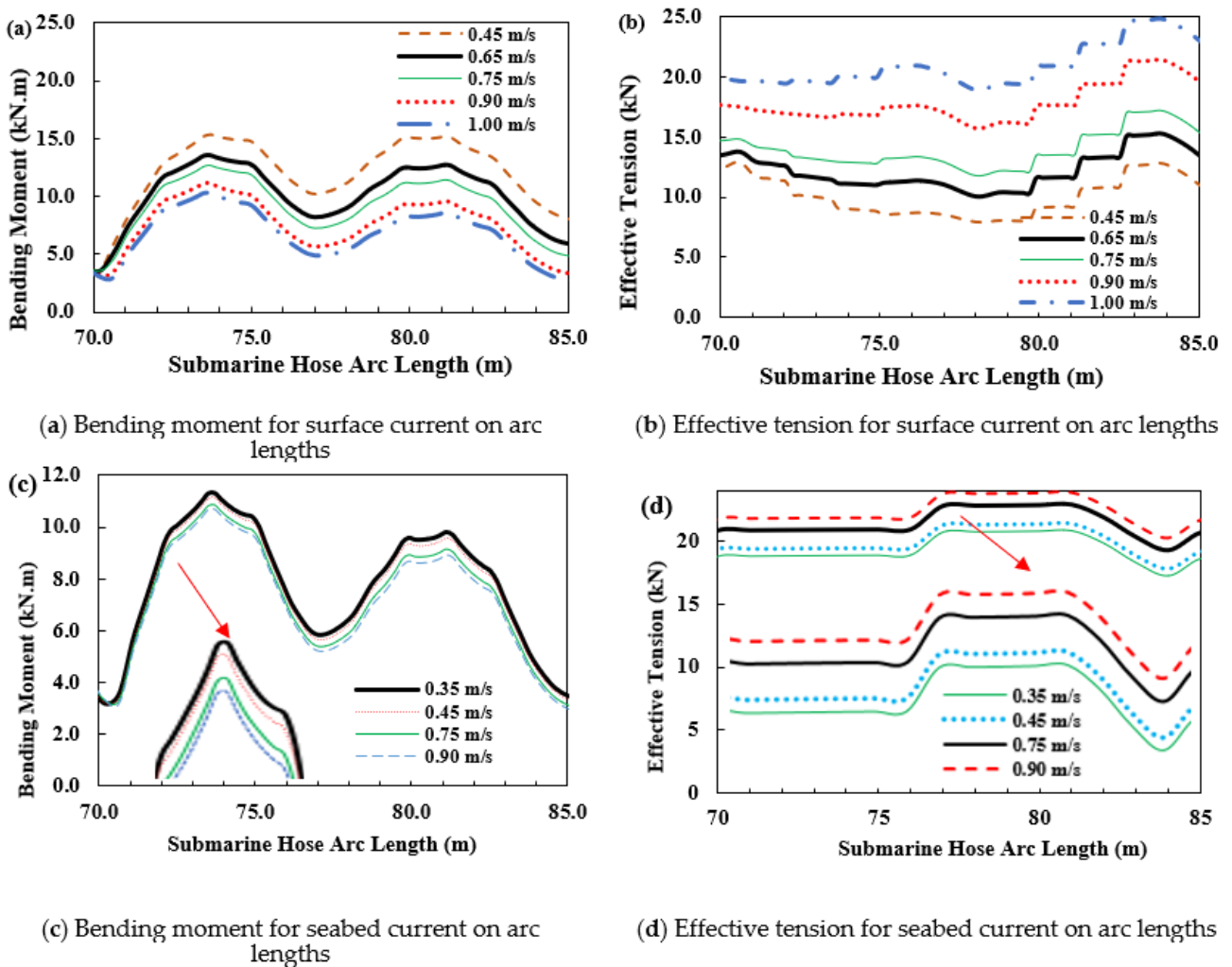


Figure 28. Influence of surface currents (a,b) and seabed currents (c,d) on submarine hoses.

4.2.4. Results of the Current Attack Angle Sensitivity on Marine Hose

The sensitivity of the current attack angle investigated on the submarine hoses in Lazy-S configuration was investigated for the following: 60°, 90°, 120°, 150° and 180°, as presented in Figure 29. It shows that the current attack on the hose-string was highest at 60°, close to the TDZ. Similarly, the 60° hose had highest effective tension at the top of the submarine hose at 123.91 kN, but had lowest tension of 3.52 kN at TDZ. Due to the nonlinear seabed profile, the effective tension may have constant distribution along the

hose arc length, but varying bending moment. This is due to the effect of the buoyancy hose on the hoses. However, the 60° model had the least amount of curvature at the top of the submarine hose.

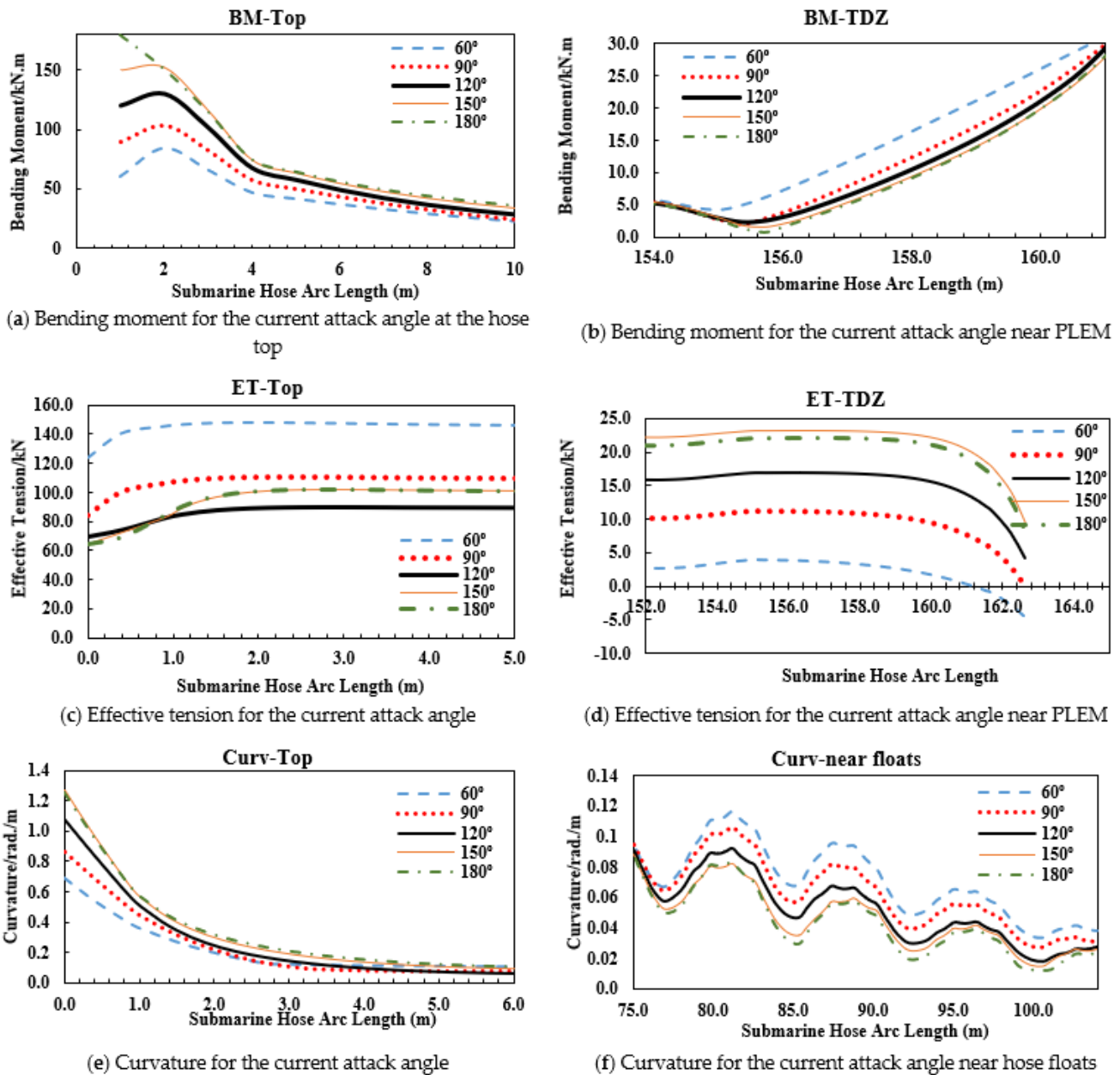


Figure 29. Influence of current attack angle on bending moment (a,b), effective tension (c,d) and curvature (e,f) on hose.

4.2.5. Results of the Time Response Sensitivity for the CALM Buoy System

The extent of the values largely depended on flow angle. A series of snapshots from the simulation in Orcaflex for Chinese-lantern configuration at 0° flow angle at $H_s = 1.87$ m, $T_z = 4.10$ s and $T_p = 5.27$ s is presented in Figure 30. It depicts the time response on the hose curvature behavior, as observed at different times, as recorded. It can be observed that the hose has snaking behavior with the highest curvature observed at time $t = 2.998$ s. As such, it is recommended to increase the reinforcement at such locations.

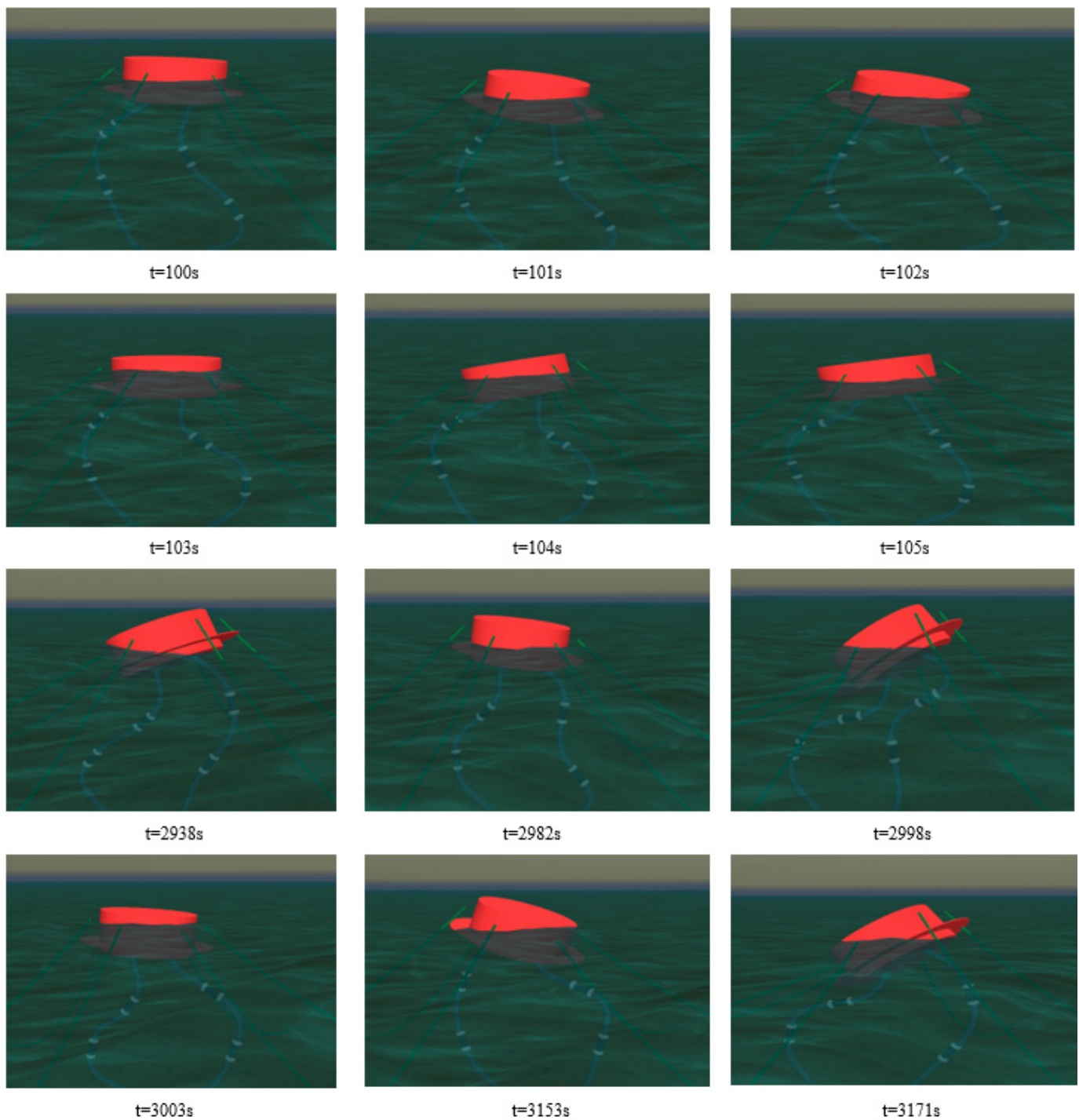


Figure 30. Snapshots of hose behavior at different times, $H_s = 1.87$ m, $T_z = 4.10$ s, 0° flow angle.

5. Further Discussion

Detailed numerical investigation on CALM buoys with submarine hoses was carried out in two configurations: Lazy-S and Chinese-lantern. It was designed under irregular waves for a cylindrical CALM buoy. The hydrodynamic panel was developed in ANSYS AQWA and solved using diffraction theory and JONSWAP Wave Spectrum for the three environmental conditions used. The boundary conditions considered for the submarine hoses were attached on the PLEM and hose manifold underneath the CALM buoy. This investigation presents the sensitivity studies on CALM buoy hose systems with improved modeling techniques on the offshore marine industry.

The offshore hose system has been modeled analytically and numerically. It was validated by considering the results of the numerical model and typical CALM buoy hose models. This study presents hydrodynamic characteristics of bending, axial force loads and the snaking phenomenon. It has been established that the contribution from each of the mooring-hose loads to the CALM buoy system influences the system's load effect. This is also a function of the ocean current, system velocity, system acceleration, azimuthal direction and the relative position of the mooring line.

From this presented investigation, the following observations were made:

1. A number of deformations were observed in the hose occurs where the MBR is high. Similarly, some curvature distributions are observed from the behavior of the submarine hoses via dynamic analysis. The models of the 0° flow angle have the highest curvatures via the arc length of the hose in both configurations. However, the 90° flow angle models reflected minimal curvature via the arc length of the hose. Damping is one method to minimize hose curvatures, in addition to inclusion of the hydrodynamic loads. It was also observed that the hoses subjected to cross-flow directions in the cases for 0° and greater curvatures developed on inclusion of the hydrodynamic loads.
2. In comparing the models for Lazy-S and Chinese-lantern configurations, while the curvature plot in the Lazy-S cases sag, the plot in the Chinese-lantern cases is hugging. Additionally, the curvatures in the Lazy-S appear to have higher curvatures; however, this can be due to the profile length of the hose-string and the azimuthal direction of the hose. However, the comparative studies on both configurations in effective tensions show that there are higher distributions recorded in the Lazy-S case than the Chinese-lantern case, but the Chinese-lantern case has more fluctuations than the Lazy-S case. This is attributed to emanate from bending in response to waves and currents. The bending moment behavior resulted from the twisting of the hose. For the bending moment cases, more undulations are observed in the Lazy-S cases than the Chinese-lantern cases, which is due to the longer length of the submarine hoses, and the floats attached on the submarine hose-string in the Lazy-S configuration.
3. It was also observed that the cross-flow model cases, particularly the case 0° and case 180° exhibited greater tensions in comparison to the case 90° . Thus, it can be deduced that an increase in the effective tension can be induced by increasing the hydromantic loads of the hose. In addition, the points of attachment of the hoses to the PLEM and to the manifold underneath the CALM buoy both exhibited maximum effective tensions that were of high magnitudes. Thus, the angle of inclination of design for the manifold is recommended to be at about 30° , as this manifold angle enhanced better results, but it is also subject to the manufacturer's choice, the environmental conditions and the marine hose properties.
4. The sensitivity of the soil characteristics shows a high significant influence on the hose-line behavior and seabed resistance on the lower end of the hose, the PLEM and any attached submarine pipeline. An increase in the soil mudline shear strength increases the seabed resistance rises steadily. This means that if submarine hoses are attached to the PLEM, there will be a noticeable dynamic lay effect. As the shear strength gradient increases, the submarine pipeline embedment will have a corresponding dynamic lay effect.
5. The sensitivity of seabed resistance on the hose-string shows that the highest soil shear stiffness of 100 kN/m/m^2 had the least bending moment, and the least effective tension under nonlinear seabed model, which shows the influence of variation or nonlinearity due to the rate of penetration, seabed soil resistance and uplift on the seabed.
6. As the surface current velocity increases, the bend radius (curvature) decreases, the bending moment decreases and the effective tension increases. Considering the seabed currents, the following seabed current velocities were considered: 0.35 m/s , 0.45 m/s , 0.75 m/s and 0.9 m/s . For the same surface current velocity, an increase in the seabed

current velocity has a reduced effective tension and reduced bending moment. An increase in the seabed current velocity gives a reduced bend radius (Curvature) and an increased effective tension and bending moment.

7. The surface wave is highly significant in the dynamic responses of the hose-line, the buoy stability and the seabed resistance. The most critical wave direction is the following sea (0° flow angle) and followed by the stern-quartering seas (30° and 60° flow angle). Naturally, an increase in wave height increases the submarine hoses' dynamic responses and seabed resistance. However, we suggest that future studies investigate the approximations analytically for the moving boundary of submarine hoses and the description of the moving boundary of submarine hoses, as such formulation is necessary for further understanding the stability and dynamics behavior.
8. This study also shows that there is a variation in the effect of the current velocity from different motion characteristics due to the resonating frequency, the effect of the current velocity is relative to the motion—if translational, such as surge and heave, or rotational, such as pitch and yaw. In the case of the heave, the frequency profile is higher from 0.299 Hz to 1.223 Hz, unlike in the surge motion where the frequency profile is 0.179 Hz to 0.278 Hz. This behavior shows a relationship between first-order wave forces and the three current velocities investigated. Similar findings were observed when current velocity was investigated for the motion RAOs of the CALM buoy.

6. Concluding Remarks

Some investigations on marine bonded hoses connected to CALM buoy have been presented on hydrodynamic characteristics, wave–current interaction and sensitivity analysis. The models were conducted for the application in shallow water and deep-water conditions. The RAO values generated from ANSYS AQWA were directly coupled to the FEM-Orcaflex model developed based on the Orcaflex Line theory. This Orcaflex line theory uses the nodes along with the hoses and mooring lines but applies some discretization for the CALM buoy. This technique aids researchers by utilizing less computational time and fewer resources. The model was validated using numerical and theoretical methods as an engineering application of the system. Different environmental conditions, mooring line conditions and hose load cases were considered in developing the model. Comparisons and sensitivity of various parameters were also conducted in this study. The investigation has also given trends and profiles for marine hoses under wind, waves and current.

The model highlights firstly include some studies on wave–current interaction, currents effects, soil strength, time response and wave loads on marine bonded hoses. Secondly, they include sensitivity analysis based on a coupled approach using the RAO from ANSYS AQWA inputted unto Orcaflex in the dynamic process. This concept has been applied to flexible risers, steel catenary risers (SCRs) and pipelay analysis. This proposed method saves computational resources, is cost-effective and has high accuracy. Thirdly, they include the global response analysis on the effect of wave angle, soil characteristics and current on the submarine hoses, which were considered under different ocean conditions. Fourthly, they include the sensitivity from the application of DAF on the offshore submarine hoses for Lazy-S and Chinese-lantern configurations with the proposed DAF_{Hose} values based on the effect of hydrodynamics loads from the buoy response on the tension of the submarine hoses based on the present study. Lastly, the model presents the motion scenario by analyzing the bending and deflection, which has an advantage in predicting the behavior of submarine hoses.

This study shows hydrodynamic characteristics of CALM buoy hose systems under wind, waves and current. It also indicates limits of tensile bending from different hose parameters on the marine hose-string, the hose behavior and the hose configuration from the sensitivity study. It discusses that these parameters influence the submarine hose configuration by providing unique curvature and tension distributions. The results of this study will also aid hose manufacturers in solving the challenge of large deformations

experienced during service operations of marine bonded hoses. Additionally, it presents an understanding of the issue of high curvature profiles experienced on marine hoses that lead to their failures. This study also contributes to the knowledge of buoy hydrodynamics under low/high amplitude waves. From this investigation, recommendations are made that will aid the improvement of buoy-hose performance. However, it is recommended that more experiments are conducted on the marine hose systems using model tests for CALM buoy systems.

Author Contributions: Conceptualization, C.V.A., F.W. and J.Y.; methodology, C.V.A., F.W. and J.Y.; software, C.V.A., F.W. and J.Y.; validation, C.V.A., F.W. and J.Y.; formal analysis, C.V.A., F.W. and J.Y.; investigation, C.V.A., F.W. and J.Y.; resources, C.V.A. and J.Y.; data curation, C.V.A., F.W. and J.Y.; writing—original draft preparation, C.V.A.; writing—review and editing, C.V.A., F.W. and J.Y.; visualization, C.V.A., F.W. and J.Y.; supervision, C.V.A., F.W. and J.Y.; project administration, C.V.A., F.W. and J.Y.; funding acquisition, C.V.A., F.W. and J.Y. All authors have read and agreed to the published version of the manuscript.

Funding: The Department of Engineering, Lancaster University, UK and EPSRC'S Doctoral Training Centre (DTC), UK are highly appreciated. In addition, the funding of Overseas Postgraduate Scholarship by Niger Delta Development Commission (NDDC), Nigeria, as well as the support of the Standards Organisation of Nigeria (SON), Nigeria are both appreciated. The research reported in this paper is part of the Project 51922064 supported by National Natural Science Foundation of China (NSFC). The article processing charges (APC) for this article was funded by Author 1-C.V.A., with the support of MDPI'S JMSE.

Institutional Review Board Statement: Not applicable.

Informed Consent Statement: Not applicable.

Data Availability Statement: The raw/processed data required to reproduce these findings cannot be shared at this time, as the data also form part of an ongoing study.

Acknowledgments: The author acknowledges the technical support from the Lancaster University Engineering Department staff. The authors also acknowledge Richard Leeuwenburgh, of Bluewater, for permission to use image of buoy in Figure 1. The authors are also grateful to Abiodun K. Oyetunji, of Lancaster University, for reviewing this manuscript. Lastly, the users support team of ANSYS and Orcaflex's Orcina, UK is appreciated for technical support.

Conflicts of Interest: The authors declare no conflict of interest. The funders had no role in the design of the study; in the collection, analyses or interpretation of data; in the writing of the manuscript, or in the decision to publish the results.

Abbreviations

ρ	Density of water
ω	Angular frequency
ω_p	Peak angular frequency
γ	Peak enhancement factor
η	The incident wave amplitude
λ	Wavelength
θ	Angle to the horizontal axis
3D	Three Dimensional
6DoF	Six Degrees of Freedom
ABS	American Bureau of Shipping
BEM	Boundary Element Method
BM	Bending Moment
BVP	Boundary Value Problem
CAD	Computer-Aided Design
CALM	Catenary Anchor Leg Mooring
CB	Cylindrical Buoy
CCS	Cartesian Coordinate System
CFD	Computational Fluid Dynamics

CMS	Conventional Mooring Systems
DAF	Dynamic Amplification Factor
DAF_{hose}	Dynamic Amplification Factor of hose
DNVGL	Det Norske Veritas & Germanischer Lloyd
FEA	Finite Element Analysis
FEM	Finite Element Model
FOS	Floating Offshore Structure
FPSO	Floating Production Storage and Offloading
FSO	Floating Storage and Offloading
GMPHOM	Guide to Manufacturing and Purchasing Hoses for Offshore Moorings
HEV	Hose End Valve
HOT	Higher Order Terms
H_s	Significant wave height
ID	Inner Diameter
JONSWAP	Joint North Sea Wave Project
IVC	Initial Boundary Condition
MBC	Marine Breakaway Coupling
MBR	Minimum Bearing Radius
MSL	Mean Sea Level
OCIMF	Oil Companies International Marine Forum
OD	Outer Diameter
PCSEMI	Paired Column Semisubmersible
PLEM	Pipeline End Manifold
QTF	Quadratic Transfer Function
RAO	Response Amplitude Operator
s	Arc length
S_B	Mean Wetted Surface
SCR	Steel Catenary Riser
SLWR	Steel Lazy Wave Catenary Risers
SPM	Single Point Mooring
TDP	Touch Down Point
TDZ	Touch Down Zone
te-m	metric tonne-meter
T_H	Horizontal tension force
T_p	Peak period
T_v	Vertical tension force
TTR	Top Tensioned Riser
T_z	Zero crossing period
VIV	Vortex Induced Vibration
VLFS	Very Large Floating Structures
WCI	Waves-Current Interaction
WEC	Wave Energy Converters
w_s	Submerged weight
WSI	Wave-Structure Interaction
x	Section length of the mooring line
z	Height above seabed

References

1. Amaechi, C.V. Novel Design, Hydrodynamics and Mechanics of Marine Hoses in Oil/Gas Applications: Case Study of Marine Hoses. Ph.D. Thesis, Engineering Department, Lancaster University, Lancaster, UK, 2022.
2. Amaechi, C.V.; Ye, J. A numerical modeling approach to composite risers for deep waters. In Proceedings of the International Conference on Composite Structures (ICCS20) Proceedings, Paris, France, 4–7 September 2017; Società Editrice Esculapio: Bologna, Italy, 2017.
3. Amaechi, C.V.; Odijie, A.C.; Sotayo, A.; Wang, F.; Hou, X.; Ye, J. Recycling of Renewable Composite Materials in the Offshore Industry. *Encycl. Renew. Sustain. Mater.* **2020**, *2*, 583–613. [[CrossRef](#)]
4. Amaechi, C.V.; Odijie, A.C.; Orok, E.O.; Ye, J. Economic Aspects of Fiber Reinforced Polymer Composite Recycling. *Encycl. Renew. Sustain. Mater.* **2020**, *2*, 377–397. [[CrossRef](#)]

5. Amaechi, C.V.; Ye, J. Local tailored design of deep water composite risers subjected to burst, collapse and tension loads. *Ocean Eng.* 2022, in press. [CrossRef]
6. Amaechi, C.V.; Ye, J. A review of state-of-the-art and meta-science analysis on composite risers for deep seas. *Ocean Eng.* 2021; under review.
7. Amaechi, C.V.; Ye, J. Development of composite risers for offshore applications with review on design and mechanics. *Ships Offshore Struct.* 2021; under review.
8. Amaechi, C.V.; Chesterton, C.; Butler, H.O.; Wang, F.; Ye, J. An Overview on Bonded Marine Hoses for sustainable fluid transfer and (un)loading operations via Floating Offshore Structures (FOS). *J. Mar. Sci. Eng.* 2021, 9, 1236. [CrossRef]
9. Amaechi, C.V.; Chesterton, C.; Butler, H.O.; Wang, F.; Ye, J. Review on the design and mechanics of bonded marine hoses for Ca-tenary Anchor Leg Mooring (CALM) buoys. *Ocean Eng.* 2021, 242, 110062. [CrossRef]
10. Ye, J.; Cai, H.; Liu, L.; Zhai, Z.; Amaechi, C.V.; Wang, Y.; Wan, L.; Yang, D.; Chen, X.; Ye, J. Microscale intrinsic properties of hybrid unidirectional/woven composite laminates: Part I experimental tests. *Compos. Struct.* 2021, 262, 113369. [CrossRef]
11. Amaechi, C.V.; Gillett, N.; Odijie, A.C.; Hou, X.; Ye, J. Composite risers for deep waters using a numerical modelling approach. *Compos. Struct.* 2019, 210, 486–499. [CrossRef]
12. Amaechi, C.V.; Gillett, N.; Odijie, A.C.; Wang, F.; Hou, X.; Ye, J. Local and Global Design of Composite Risers on Truss SPAR Platform in Deep waters. In Proceedings of the 5th International Conference on Mechanics of Composites, Instituto Superior de Tecnico, Lisbon, Portugal, 1–4 July 2019; No. 20005. pp. 1–3. Available online: https://eprints.lancs.ac.uk/id/eprint/136431/4/Local_and_Global_analysis_of_Composite_Risers_MechComp2019_Conference_Victor.pdf (accessed on 19 May 2021).
13. Amaechi, C.V.; Adefuye, E.F.; Oyetunji, A.K.; Ja'e, I.A.; Adelusi, I.; Odijie, A.C.; Wang, F. Numerical Study on Plastic Strain Distributions and Mechanical Behaviour of a Tube under Bending. *Inventions* 2022, 7, 9. [CrossRef]
14. Wang, F. Effective design of submarine pipe-in-pipe using Finite Element Analysis. *Ocean Eng.* 2018, 153, 23–32. [CrossRef]
15. Wang, F.-C.; Han, L.-H. Analytical behavior of carbon steel-concrete-stainless steel double-skin tube (DST) used in submarine pipeline structure. *Mar. Struct.* 2019, 63, 99–116. [CrossRef]
16. Wang, F.-C.; Han, L.-H.; Li, W. Analytical behavior of CFDST stub columns with external stainless steel tubes under axial compression. *Thin-Walled Struct.* 2018, 127, 756–768. [CrossRef]
17. Wang, J.-T.; Wang, F.-C. Analytical behavior of built-up square concrete-filled steel tubular columns under combined preload and axial compression. *Steel Compos. Struct.* 2021, 38, 617–635. [CrossRef]
18. EMSTEC. *EMSTEC Loading & Discharge Hoses for Offshore Moorings*; EMSTEC: Rosengarten, Germany, 2016. Available online: <https://denialink.eu/pdf/emstec.pdf> (accessed on 29 September 2021).
19. Yokohama. *Seaflex Yokohama Offshore Loading & Discharge Hose*; The Yokohama Rubber Co. Ltd.: Hiratsuka City, Japan, 2016. Available online: <https://www.y-yokohama.com/global/product/mb/pdf/resource/seaflex.pdf> (accessed on 17 May 2021).
20. Amaechi, C.V.; Wang, F.; Ye, J. Numerical studies on CALM buoy motion responses and the effect of buoy geometry cum skirt dimensions with its hydrodynamic waves-current interactions. *Ocean Eng.* 2021, 244, 110378. [CrossRef]
21. Amaechi, C.V.; Chesterton, C.; Odijie, A.C.; Ye, J. Numerical assessment of offshore hose load response during reeling and free-hanging operations under ocean waves. *Ocean Eng.* 2021; under review.
22. Amaechi, C.V.; Chesterton, C.; Butler, H.O.; Gu, Z.; Odijie, A.C.; Wang, F. Finite element modelling on the mechanical behaviour of Marine Bonded Composite Hose (MBCH) under burst and collapse. *J. Mar. Sci. Eng.* 2022, 10, under review.
23. Amaechi, C.V.; Wang, F.; Ye, J. Understanding the fluid-structure interaction from wave diffraction forces on CALM buoys: Numerical and analytical solutions. *Ships Offshore Struct.* 2021. [CrossRef]
24. Amaechi, C.V.; Wang, F.; Ye, J. Numerical Assessment on the Dynamic Behaviour of Submarine Hoses Attached to CALM Buoy Configured as Lazy-S under Water Waves. *J. Mar. Sci. Eng.* 2021, 9, 1130. [CrossRef]
25. Amaechi, C.V.; Wang, F.; Ye, J. Experimental study on motion characterization of CALM buoy hose system under water waves. *J. Mar. Sci. Eng.* 2022; under review.
26. Amaechi, C.V.; Wang, F.; Ye, J. An investigation on the vortex effect of a CALM buoy under water waves using Computational Fluid Dynamics (CFD). *Inventions*, 2022; under review.
27. Odijie, A.C.; Ye, J. Effect of Vortex Induced Vibration on a Paired-Column Semisubmersible Platform. *Int. J. Struct. Stab. Dyn.* 2015, 15, 1540019. [CrossRef]
28. Odijie, A.C.; Wang, F.; Ye, J. A review of floating semisubmersible hull systems: Column stabilized unit. *Ocean Eng.* 2017, 144, 191–202. [CrossRef]
29. Odijie, A.C.; Ye, J. Understanding Fluid-Structure Interaction for high amplitude wave loadings on a deep-draft paired column semi-submersible platform: A finite element approach. In Proceedings of the International Conference on Light Weight Design of Marine Structures, Glasgow, UK, 9–11 November 2015.
30. Amaechi, C.V.; Odijie, A.C.; Wang, F.; Ye, J. Parametric investigation on tensioner stroke analysis, recoil analysis and disconnect for the marine drilling riser of a Paired Column Semisubmersible under deep water waves. *Ocean Eng.* 2021; under review.
31. Amaechi, C.V.; Wang, F.; Ye, J. Dynamic analysis of tensioner model applied on global response of marine riser recoil and disconnect. *Ocean Eng.* 2022; under review.
32. Odijie, A.C.; Quayle, S.; Ye, J. Wave induced stress profile on a paired column semisubmersible hull formation for column reinforcement. *Eng. Struct.* 2017, 143, 77–90. [CrossRef]

33. Amaechi, C.V.; Odijie, A.C.; Wang, F.; Ye, J. Numerical investigation on mooring line configurations of a Paired Column Semisubmersible for its global performance in deep water condition. *Ocean Eng.* **2021**. [CrossRef]
34. OCIMF. *Guide to Manufacturing and Purchasing Hoses for Offshore Moorings (GMPHOM)*; Witherby Seamanship International Ltd.: Livingstone, UK, 2009.
35. OCIMF. *Guideline for the Handling, Storage, Inspection and Testing of the Hose*, 2nd ed.; Witherby & Co. Ltd.: London, UK, 1995.
36. OCIMF. *Single Point Mooring Maintenance and Operations Guide (SMOG)*; Witherby & Co. Ltd.: London, UK, 1995.
37. Amaechi, C.V. Single Point Mooring (SPM) Hoses and Catenary Anchor Leg Mooring (CALM) Buoys. LinkedIn Pulse. Published on 26 July 2021. Available online: <https://www.linkedin.com/pulse/single-point-mooring-spm-hoses-catenary-anchor-leg-calm-amaechi> (accessed on 1 September 2021).
38. Trelleborg. Trelleborg Fluid Handling Solutions. Oil & Marine Hoses: Innovation and Safety for Oil & Gas Transfer Systems. In *Trelleborg Oil & Gas Solutions: Oil & Gas Hoses for Enhanced Fluid Transfer Solutions*; Trelleborg: Clermont-Ferrand, France, 2018; Volume 1, pp. 1–30.
39. Bluewater Energy Services. *Buoyed Up: The Future of Tanker Loading/Offloading Operations*; Bluewater Energy Services: Amsterdam, The Netherlands, 2009. Available online: <https://www.bluewater.com/wp-content/uploads/2013/04/CALM-Buoy-brochure-English.pdf> (accessed on 18 July 2021).
40. Continental. Marine Hose Brochure. 2020. Available online: https://aosoffshore.com/wp-content/uploads/2020/02/ContiTech_Marine-Brochure.pdf (accessed on 17 February 2021).
41. Trelleborg. Surface Buoyancy. Trelleborg Marine and Infrastructure: Product Brochure. Ref.: BC-SUR-v1.3. Trelleborg Sweden. 2017. Available online: <https://www.trelleborg.com/en/marine-and-infrastructure/products-solutions-and-services/marine/surface-buoyancy> (accessed on 30 September 2021).
42. Bluewater Energy Services. *Oceans of Knowledge*; Bluewater Energy Services: Amsterdam, The Netherlands, 2019; pp. 1–20.
43. OIL. *Offloading Hoses: Floating & Submarine Hoses-OIL Hoses Brochure*; Offspring International Limited: Dudley, UK, 2014. Available online: <https://www.offspringinternational.com/wp-content/uploads/2020/06/OIL-Offloading-Hoses-Brochure-2020-W.pdf> (accessed on 12 July 2021).
44. OIL. *Mooring and Offloading Systems*; Offspring International Limited: Dudley, UK, 2015. Available online: <https://www.offspringinternational.com/wp-content/uploads/2015/04/OIL-SPM-Brochure-2015.pdf> (accessed on 12 July 2021).
45. Bluewater. *Conventional Buoy Mooring Systems*; Bluewater Energy Services: Amsterdam, The Netherlands, 2009.
46. Bluewater. *Turret Buoy*; Bluewater Energy Services: Amsterdam, The Netherlands, 2016.
47. ContiTech. Marine Hoses-Offshore Fluid Transfer. Contitech Oil & Gas, UK. 2017. Available online: http://www.contitech-oil-gas.com/pages/marine-hoses/marine-hoses_en.html (accessed on 30 September 2021).
48. ContiTech. *High Performance Flexible Hoses Brochure*; Contitech Oil & Gas: Grimsby, UK, 2014.
49. Bluewater. *Bluewater Turret Buoy-Technical Description*; Bluewater Energy Services: Amsterdam, The Netherlands, 2011.
50. Constantin, A.; Ivanov, R.; Martin, C.I. Hamiltonian Formulation for Wave-Current Interactions in Stratified Rotational Flows. *Arch. Ration. Mech. Anal.* **2016**, *221*, 1417–1447. [CrossRef]
51. Chen, Y.; Chen, L.; Zhang, H.; Gong, W. Effects of wave-current interaction on the Pearl River Estuary during Typhoon Hato. *Estuar. Coast. Shelf Sci.* **2019**, *228*, 106364. [CrossRef]
52. Hegermiller, C.A.; Warner, J.C.; Olabarrieta, M.; Sherwood, C.R. Wave-Current Interaction between Hurricane Matthew Wave Fields and the Gulf Stream. *J. Phys. Oceanogr.* **2019**, *49*, 2883–2900. [CrossRef]
53. Jia, L.; Ren, J.; Nie, D.; Chen, B.; Lv, X. Wave-current bottom shear stresses and sediment re-suspension in the mouth bar of the Modaomen Estuary during the dry season. *Acta Oceanol. Sin.* **2014**, *33*, 107–115. [CrossRef]
54. Beya, I.; Buckham, B.; Robertson, B. Impact of tidal currents and model fidelity on wave energy resource assessments. *Renew. Energy* **2021**, *176*, 50–66. [CrossRef]
55. Odijie, A.C. Design of Paired Column Semisubmersible Hull. Ph.D. Thesis, Engineering Department, Lancaster University, Lancaster, UK, 2016. Available online: <https://eprints.lancs.ac.uk/id/eprint/86961/1/2016AgbomeriePhD.pdf> (accessed on 12 February 2020).
56. Mohamed, H.A.M.A. Hydrodynamic Loading and Responses of Semisubmersibles. Ph.D. Thesis, School of Marine Science and Technology, Newcastle University, Newcastle upon Tyne, UK, 2011. Available online: <https://theses.ncl.ac.uk/jspui/bitstream/10443/1285/1/Hassan%20Mohamed%202011.pdf> (accessed on 6 October 2021).
57. Chen, L.; Basu, B. Fatigue load estimation of a spar-type floating offshore wind turbine considering wave-current interactions. *Int. J. Fatigue* **2018**, *116*, 421–428. [CrossRef]
58. Henriques, T.D.J.; Tedds, S.; Botsari, A.; Najafian, G.; Hedges, T.; Sutcliffe, C.; Owen, I.; Poole, R. The effects of wave-current interaction on the performance of a model horizontal axis tidal turbine. *Int. J. Mar. Energy* **2014**, *8*, 17–35. [CrossRef]
59. Hirdaris, S.; Bai, W.; Dessi, D.; Ergin, A.; Gu, X.; Hermundstad, O.; Huijsmans, R.; Iijima, K.; Nielsen, U.; Parunov, J.; et al. Loads for use in the design of ships and offshore structures. *Ocean Eng.* **2013**, *78*, 131–174. [CrossRef]
60. Bai, Y.; Bai, Q. *Subsea Pipelines and Risers*, 1st ed.; Elsevier: Oxford, UK, 2005.
61. Bai, Y.; Bai, Q. *Subsea Engineering Handbook*; Elsevier: Oxford, UK, 2010.
62. Wichers, I.J. *Guide to Single Point Moorings*; WMooring Inc.: Houston, TX, USA, 2013. Available online: http://www.wmooring.com/files/Guide_to_Single_Point_Moorings.pdf (accessed on 18 December 2021).
63. Berteaux, H.O. *Buoy Engineering*; John Wiley and Sons: New York, NY, USA, 1976.

64. Berteaux, H.O.; Goldsmith, R.A.; Schott, W.E., III. *Heave and Roll Response of Free Floating Bodies of Cylindrical Shape*; Report WHOI-77-12; Woods Hole Oceanographic Institution: Massachusetts, MA, USA, 1977. Available online: <https://apps.dtic.mil/sti/pdfs/ADA038215.pdf> (accessed on 15 August 2021).
65. Wilson, J.F. *Dynamics of Offshore Structures*, 2nd ed.; John Wiley and Sons: Hoboken, NJ, USA, 2003.
66. Sorensen, R.M. *Basic Coastal Engineering*, 3rd ed.; Springer: New York, NY, USA, 2006.
67. Sorensen, R.M. *Basic Wave Mechanics: For Coastal and Ocean Engineers*; John Wiley and Sons: London, UK, 1993.
68. Havelock, T.H. The pressure of water waves upon a fixed obstacle. *Proc. R. Soc. Lond. Ser. A Math. Phys. Sci.* **1940**, *175*, 409–421. [[CrossRef](#)]
69. MacCamy, R.C.; Fuchs, R.A. *Wave Forces on Piles: A Diffraction Theory*; Report BEB-TM-69; Beach Erosion Board, Department of Army: Washington, DC, USA, 1954; pp. 1–17. Available online: <https://erdc-library.erdc.dren.mil/jspui/bitstream/11681/3444/1/BEB-TM-69.pdf> (accessed on 8 September 2021).
70. Chakrabarti, S.K. Nonlinear wave forces on vertical cylinder. *J. Hydraul. Div.* **1972**, *98*, 1895–1909. [[CrossRef](#)]
71. Chakrabarti, S.K. Second-Order Wave Force on Large Vertical Cylinder. *J. Waterw. Harb. Coast. Eng. Div.* **1975**, *101*, 311–317. [[CrossRef](#)]
72. Rahman, M. Non-linear wave loads on large circular cylinders: A perturbation technique. *Adv. Water Resour.* **1981**, *4*, 9–19. [[CrossRef](#)]
73. Rahman, M. Second order wave interaction with large structures. In *Wave Phenomena: Modern Theory and Applications*; Rogers, T.B.M.C., Ed.; North-Holland Mathematics Studies; Elsevier B.V: North Holland, The Netherlands, 1984; Volume 97, pp. 49–69. [[CrossRef](#)]
74. Newman, J.N. The second-order wave force on a vertical cylinder. *J. Fluid Mech.* **1996**, *320*, 417–443. [[CrossRef](#)]
75. Ghalayini, S.; Williams, A. Nonlinear wave forces on vertical cylinder arrays. *J. Fluids Struct.* **1991**, *5*, 1–32. [[CrossRef](#)]
76. Zhang, S.-F.; Chen, C.; Zhang, Q.-X.; Zhang, N.-M.; Zhang, F. Wave Loads Computation for Offshore Floating Hose Based on Partially Immersed Cylinder Model of Improved Morison Formula. *Open Pet. Eng. J.* **2015**, *8*, 130–137. [[CrossRef](#)]
77. Liu, B.; Fu, D.; Zhang, Y.; Chen, X. Experimental and numerical study on the wave force calculation of a partially immersed horizontal cylindrical float. *Int. J. Nav. Arch. Ocean Eng.* **2020**, *12*, 733–742. [[CrossRef](#)]
78. Morison, J.; Johnson, J.; Schaaf, S. The Force Exerted by Surface Waves on Piles. *J. Pet. Technol.* **1950**, *2*, 149–154. [[CrossRef](#)]
79. Brebbia, C.A.; Walker, S. *Dynamic Analysis of Offshore Structures*, 2013 Reprint of 1979 ed.; Newnes-Butterworth & Co. Publishers Ltd.: London, UK, 2013.
80. Sarpkaya, T. *Wave Forces on Offshore Structures*, 1st ed.; Cambridge University Press: New York, NY, USA, 2014.
81. Chandrasekaran, S. *Dynamic Analysis and Design of Offshore Structures*, 1st ed.; Springer: New Delhi, India, 2015.
82. Chandrasekaran, S.; Jain, A.K.; Chandak, N.R. Response Behavior of Triangular Tension Leg Platforms under Regular Waves Using Stokes Nonlinear Wave Theory. *J. Waterw. Port Coast. Ocean Eng.* **2007**, *133*, 230–237. [[CrossRef](#)]
83. Chakrabarti, S.K. *Handbook of Offshore Engineering*; Elsevier: Oxford, UK, 2005; Volume 1.
84. Amaechi, C.V.; Wang, F.; Ja’e, I.A.; Aboshio, A.; Odijie, A.C.; Ye, J. A literature review on the technologies of bonded hoses for marine applications. *Ships Offshore Struct.* **2022**. [[CrossRef](#)]
85. Cozijn, J.L.; Bunnik, T.H.J. Coupled Mooring Analysis for a Deep Water CALM Buoy. In Proceedings of the 23rd International Conference on Offshore Mechanics and Arctic Engineering (OMAE), Vancouver, BC, Canada, 20–25 June 2004; OMAE2004-51370; Volume 1, Parts A and B. The American Society of Mechanical Engineers (ASME): New York, NY, USA, 2004; pp. 663–673. [[CrossRef](#)]
86. Cozijn, H.; Uittenbogaard, R.; Brake, E.T. Heave, Roll and Pitch Damping of a Deepwater CALM Buoy with a Skirt. In Proceedings of the International Society of Offshore and Polar Engineering Conference (ISOPE) Proceedings, Seoul, Korea, 19–24 June 2005; ISOPE: Cupertino, CA, USA, 2005; Volume 8, pp. 388–395. Available online: https://www.researchgate.net/publication/267364857_Heave_Roll_and_Pitch_Damping_of_a_Deepwater_CALM_Buoy_with_a_Skirt (accessed on 11 September 2021).
87. Rahman, M.; Chakravartty, I.C. Hydrodynamic Loading Calculations for Offshore Structures. *SIAM J. Appl. Math.* **1981**, *41*, 445–458. [[CrossRef](#)]
88. Raman, H.; Venkatanarasaiah, P. Forces due to Nonlinear Waves on Vertical Cylinders. *J. Waterw. Harb. Coast. Eng. Div.* **1976**, *102*, 301–316. [[CrossRef](#)]
89. Bhatta, D.; Rahman, M. On scattering and radiation problem for a cylinder in water of finite depth. *Int. J. Eng. Sci.* **2003**, *41*, 931–967. [[CrossRef](#)]
90. Lighthill, J. Waves and hydrodynamic loading. In Proceedings of the 2nd International Conference on the Behavior of Offshore Structures (BOSS ’79), London, UK, 28–31 August 1979; pp. 1–40.
91. Lighthill, J. Fundamentals concerning wave loading on offshore structures. *J. Fluid Mech.* **1986**, *173*, 667–681. [[CrossRef](#)]
92. Brown, M.; Elliott, L. Two-dimensional dynamic analysis of a floating hose string. *Appl. Ocean Res.* **1988**, *10*, 20–34. [[CrossRef](#)]
93. Brown, M.J. Mathematical Model of a Marine Hose-String at a Buoy—Part 1—Static Problem. In *Offshore and Coastal Modelling*; Dyke, P., Moscardini, A.O., Robson, E.H., Eds.; Springer: London, UK, 1985; pp. 251–277. [[CrossRef](#)]
94. Brown, M.J. Mathematical Model of a Marine Hose-String at a Buoy—Part 2—Dynamic Problem. In *Offshore and Coastal Modelling*; Dyke, P., Moscardini, A.O., Robson, E.H., Eds.; Springer: London, UK, 1985; pp. 279–301. [[CrossRef](#)]
95. Huang, T.S.; Leonard, J.W. Lateral Stability of a Flexible Submarine Hoseline, Port Hueneme, California, USA. 1989. Available online: <https://apps.dtic.mil/sti/pdfs/ADA219251.pdf> (accessed on 8 September 2021).

96. Bree, J.; Halliwell, A.R.; O'Donoghue, T. Snaking of Floating Marine Oil Hose Attached to SPM Buoy. *J. Eng. Mech.* **1989**, *115*, 265–284. [[CrossRef](#)]
97. O'Donoghue, T.; Halliwell, A.R. Floating Hose-Strings Attached to a CALM Buoy. In Proceedings of the Offshore Technology Conference, Houston, TX, USA, 2–5 May 1988; OTC 5717. pp. 313–320. [[CrossRef](#)]
98. O'Donoghue, T.; Halliwell, A. Vertical bending moments and axial forces in a floating marine hose-string. *Eng. Struct.* **1990**, *12*, 124–133. [[CrossRef](#)]
99. O'Donoghue, T. The Dynamic Behaviour of a Surface Hose Attached to a CALM Buoy. Ph.D. Thesis, Department of Offshore Engineering, Heriot-Watt University, Edinburgh, UK, 1987. Available online: https://www.ros.hw.ac.uk/bitstream/10399/1045/1/O%27DonoghueT_0587_epsBL.pdf (accessed on 1 September 2021).
100. Amaechi, C.V.; Wang, F.; Ye, J. Mathematical Modelling of Bonded Marine Hoses for Single Point Mooring (SPM) Systems, with Catenary Anchor Leg Mooring (CALM) Buoy application—A Review. *J. Mar. Sci. Eng.* **2021**, *9*, 1179. [[CrossRef](#)]
101. Edward, C.; Dev, A.K. Assessment of CALM Buoys Motion Response and Dominant OPB/IPB Inducing Parameters on Fatigue Failure of Offshore Mooring Chains. In *Practical Design of Ships and Other Floating Structures. PRADS 2019. Lecture Notes in Civil Engineering*; Okada, T., Suzuki, K., Kawamura, Y., Eds.; Springer: Singapore, 2021; Volume 64. [[CrossRef](#)]
102. Bridgestone. *Study of Causes of Kinking in Floating Hoses at Petrobras/Tefran Terminal*; Report No. 6YMT-0011; Bridgestone: Kurume, Japan, 1976.
103. Denney, D. Chain Failure by Bending on Deepwater Mooring Systems. *J. Pet. Technol.* **2006**, *58*, 72–73. [[CrossRef](#)]
104. Brady, I.; Williams, S.; Golby, P. A study of the Forces Acting on Hoses at a Monobuoy Due to Environmental Conditions. In Proceedings of the Offshore Technology Conference Proceeding—OTC 2136, Dallas, TX, USA, 5–7 May 1974; pp. 1–10. [[CrossRef](#)]
105. Ryu, S.; Duggal, A.S.; Heyl, C.N.; Liu, Y. Prediction of Deepwater Oil Offloading Buoy Response and Experimental Validation. *Int. J. Offshore Polar Eng.* **2006**, *16*, 1–7. Available online: https://www.sofec.com/wp-content/uploads/white_papers/2006-ISOPE-Prediction-of-DW-Oil-Offloading-Buoy-Response.pdf (accessed on 11 September 2021).
106. Duggal, A.; Ryu, S. The dynamics of deepwater offloading buoys. In *WIT Transactions on the Built Environment*; Paper FSI05026FU; WIT Press: Singapore, 2005. Available online: <https://www.witpress.com/Secure/elibrary/papers/FSI05/FSI05026FU.pdf> (accessed on 6 July 2021).
107. Le Cunff, C.; Ryu, S.; Duggal, A.S.; Ricbourg, C.; Heurtier, J.; Heyl, C.; Liu, Y.; Beauclair, O. Derivation of CALM Buoy coupled motion RAOs in Frequency Domain and Experimental Validation. In Proceedings of the International Society of Offshore and Polar Engineering Conference Proceedings, Lisbon, Portugal, 1–6 July 2007; ISOPE: Lisbon, Portugal, 2007; pp. 1–8. Available online: https://www.sofec.com/wp-content/uploads/white_papers/2007-ISOPE-Derivation-of-CALM-Buoy-Coupled-Motion-RAOs-in-Frequency-Domain.pdf (accessed on 11 September 2021).
108. Le Cunff, C.; Ryu, S.; Heurtier, J.; Duggal, A.S. Frequency-Domain Calculations of Moored Vessel Motion Including Low Frequency Effect. In Proceedings of the ASME 2008 27th International Conference on Offshore Mechanics and Arctic Engineering, Volume 1: Offshore Technology, Estoril, Portugal, 15–20 June 2008; pp. 689–696. [[CrossRef](#)]
109. Wang, F.-C.; Wang, J.; Tang, K. A finite element based study on lowering operation of subsea massive structure. *China Ocean Eng.* **2017**, *31*, 646–652. [[CrossRef](#)]
110. Lenci, S.; Callegari, M. Simple analytical models for the J-lay problem. *Acta Mech.* **2005**, *178*, 23–39. [[CrossRef](#)]
111. Hasanvand, E.; Edalat, P. Sensitivity Analysis of the Dynamic Response of CALM Oil Terminal, in The Persian Gulf Region Under Different Operation Parameters. *Mar. Eng.* **2020**, *16*, 73–84. [[CrossRef](#)]
112. Senra, S.F.; Jacob, B.P.; Torres, F.L.; Lúcia, A.; Mourelle, M.M. Sensitivity Studies On the Fatigue Behavior of Steel Catenary Risers. In Proceedings of the Twelfth International Offshore and Polar Engineering Conference, Kitakyushu, Japan, 26–31 May 2002. Paper Number: ISOPE-I-02-162.
113. Pecher, A.; Foglia, A.; Kofoed, J.P. Comparison and Sensitivity Investigations of a CALM and SALM Type Mooring System for Wave Energy Converters. *J. Mar. Sci. Eng.* **2014**, *2*, 93–122. [[CrossRef](#)]
114. Sun, H.; Wang, D. Sensitivity Analysis of Buoyancy Modules Parameters of Lazy-Wave Flexible Riser. In Proceedings of the ASME 2013 32nd International Conference on Ocean, Offshore and Arctic Engineering, Volume 4A: Pipeline and Riser Technology, Nantes, France, 9–14 June 2013; p. V04AT04A037. [[CrossRef](#)]
115. Amaechi, C.V.; Ye, J.; Hou, X.; Wang, F.-C. Sensitivity Studies on Offshore Submarine Hoses on CALM Buoy with Comparisons for Chinese-Lantern and Lazy-S Configuration OMAE2019-96755. In Proceedings of the 38th International Conference on Ocean, Offshore and Arctic Engineering, Glasgow, UK, 9–14 June 2019; American Society of Mechanical Engineers: New York, NY, USA, 2019. Available online: <https://eprints.lancs.ac.uk/id/eprint/134404> (accessed on 18 December 2021).
116. Bidgoli, S.I.; Shahriari, S.; Edalat, P. Sensitive Analysis of Different Types of Deep Water Risers to Conventional Mooring Systems. *Int. J. Coast. Offshore Eng.* **2017**, *5*, 37–47.
117. Axelsson, G.; Skjerve, H. Flexible Riser Carcass Collapse Analyses: Sensitivity on Radial Gaps and Bending. In Proceedings of the ASME 2014 33rd International Conference on Ocean, Offshore and Arctic Engineering, Volume 6A: Pipeline and Riser Technology, San Francisco, CA, USA, 8–13 June 2014; p. V06AT04A059. [[CrossRef](#)]
118. Tang, L.; Huang, Z.; Zhu, X.; Zhou, Y.; Li, B. Investigation of the mechanical response of a deep-water drilling riser to ocean currents and waves. *Adv. Mech. Eng.* **2019**, *11*, 1–11. [[CrossRef](#)]
119. Zhang, J.; Guo, H.; Tang, Y.; Li, Y. Effect of Top Tension on Vortex-Induced Vibration of Deep-Sea Risers. *J. Mar. Sci. Eng.* **2020**, *8*, 121. [[CrossRef](#)]

120. Li, F.Z.; Low, Y.M. Sensitivity Study of Critical Parameters Influencing the Uncertainty of Fatigue Damage in Steel Catenary Risers. In Proceedings of the ASME 2010 29th International Conference on Ocean, Offshore and Arctic Engineering, Shanghai, China, 6–11 June 2010; Volume 2, pp. 31–39. [CrossRef]
121. Yang, H.; Li, H. Sensitivity analysis of fatigue life prediction for deepwater steel lazy wave catenary risers. *Sci. China Technol. Sci.* **2011**, *54*, 1881–1887. [CrossRef]
122. Wang, K.; Ji, C.; Xue, H.; Tang, W. Fatigue sensitivity analysis of steel catenary riser near touchdown point. *J. Shanghai Jiaotong Univ. (Sci.)* **2017**, *22*, 570–576. [CrossRef]
123. Quéau, L.M.; Kimiaei, M.; Randolph, M. Sensitivity studies of SCR fatigue damage in the touchdown zone using an efficient simplified framework for stress range evaluation. *Ocean Eng.* **2015**, *96*, 295–311. [CrossRef]
124. Yoo, K.-K.; Joo, Y. Sensitivity Study on SCR Design for Spread-Moored FPSO in West Africa. *J. Ocean Eng. Technol.* **2017**, *31*, 111–120. [CrossRef]
125. ANSYS. *ANSYS Aqwa Theory Manual*; Release 18.2; ANSYS Inc.: Canonsburg, PA, USA, 2017.
126. ANSYS. *ANSYS Aqwa User's Manual*; Release 18.2; ANSYS Inc.: Canonsburg, PA, USA, 2017.
127. Orcina. *OrcaFlex Manual*; Version 9.8a; Orcina Ltd.: Ulverton, Cumbria, UK, 2014. Available online: <https://www.orcina.com/webhelp/OrcaFlex/Default.htm> (accessed on 16 February 2020).
128. Orcina. Orcaflex Help Manual, Version 11.0f. 2021. Available online: <https://www.orcina.com/SoftwareProducts/OrcaFlex/Documentation/index.php> (accessed on 20 July 2021).
129. Orcina. Orcaflex Help Manual—Line with Floats: Added Mass Coefficients. 2019. Available online: <https://www.orcina.com/webhelp/OrcaFlex/Content/html/Linewithfloats,Addedmasscoefficients.htm> (accessed on 20 July 2021).
130. Wang, D.; Sun, S. Study of the radiation problem for a CALM buoy with skirt. *Ship Build. China* **2015**, *56*, 95–101.
131. Ruan, W.; Shi, J.; Sun, B.; Qi, K. Study on fatigue damage optimization mechanism of deepwater lazy wave risers based on multiple waveform serial arrangement. *Ocean Eng.* **2021**, *228*, 108926. [CrossRef]
132. DNVGL. *DNVGL-RP-F205 Global Performance Analysis of Deepwater Floating Structures*; Det Norske Veritas & Germanischer Lloyd: Oslo, Norway, 2017.
133. DNVGL. *DNVGL-RP-N103 Modelling and Analysis of Marine Operations*; Det Norske Veritas & Germanischer Lloyd: Oslo, Norway, 2017.
134. DNVGL. *DNVGL-OS-E403 Offshore Loading Buoys*; Det Norske Veritas & Germanischer Lloyd: Oslo, Norway, 2015.
135. ABS. *Rules for Building and Classing—Single Point Moorings*; American Bureau of Shipping: New York, NY, USA, 2017; Volume 2017.
136. Hasselmann, K.; Barnett, T.P.; Bouws, E.; Carlson, H.; Cartwright, D.E.; Enke, K.; Ewing, J.A.; Gienapp, H.; Hasselmann, D.E.; Kruseman, P.; et al. Measurements of wind-wave growth and swell decay during the Joint North Sea Wave Project (JONSWAP). In *Ergänzungsheft zur Dtsch. Hydrogr. Z. -Hydraulic Engineering Reports; Ergänzungsheft 8-12; Reihe Vol. A80, Issue 12*; Deutsches Hydrographisches Institut.: Hamburg, Germany, 1973; Volume 12, pp. 1–90. Available online: <http://resolver.tudelft.nl/uuid:f204e188-13b9-49d8-a6dc-4fb7c20562fc> (accessed on 4 March 2021).
137. Chibueze, N.O.; Ossia, C.V.; Okoli, J.U. On the Fatigue of Steel Catenary Risers. *Stroj. Vestn. J. Mech. Eng.* **2016**, *62*, 751–756. [CrossRef]
138. Vyzikas, T. *Application of Numerical Models and Codes; A Best Practice Report Prepared as Part of the MERIFIC Project—Marine Energy in Far Peripheral and Island Communities (MERIFIC)*; University of Plymouth: Plymouth, UK, 2014; pp. 56–60.
139. Chakrabarti, S.K. Technical Note: On the formulation of Jonswap spectrum. *Appl. Ocean Res.* **1984**, *6*, 175–176. [CrossRef]
140. Isherwood, R. Technical note: A revised parameterisation of the Jonswap spectrum. *Appl. Ocean Res.* **1987**, *9*, 47–50. [CrossRef]
141. Pierson, W.J., Jr.; Moskowitz, L. A proposed spectral form for fully developed wind seas based on the similarity theory of S. A. Kitaigorodskii. *J. Geophys. Res. Space Phys.* **1964**, *69*, 5181–5190. [CrossRef]
142. Sparks, C.P. *Fundamentals of Marine Riser Mechanics: Basic Principles and Simplified Analyses*, 2nd ed.; PennWell Books: Tulsa, OK, USA, 2018.
143. Dareing, D.W. *Mechanics of Drillstrings and Marine Risers*, 1st ed.; ASME Press: New York, NY, USA, 2012. [CrossRef]
144. Irvine, H.M. *Cable Structures*; MIT Press: Cambridge, MA, USA, 1981.
145. Fergestad, D.; Løvteit, S.A. *Handbook on Design and Operation of Flexible Pipes; MARINTEK/NTNU/4Subsea*, 3rd ed.; Sintef: Trondheim, Norway, 2017; ISBN 978-82-7174-285-0. Available online: https://www.4subsea.com/wp-content/uploads/2017/07/Handbook-2017_Flexible-pipes_4Subsea-SINTEF-NTNU_lo-res.pdf (accessed on 25 August 2021).
146. Amaechi, C.V.; Wang, F.; Hou, X.; Ye, J. Strength of submarine hoses in Chinese-lantern configuration from hydrodynamic loads on CALM buoy. *Ocean Eng.* **2019**, *171*, 429–442. [CrossRef]
147. Roveri, F.E.; Volnei, S.; Sagrilo, L.; Cicilia, F.B. A Case Study on the Evaluation of Floating Hose Forces in a C.A.L.M. System. In Proceedings of the 12th International Offshore and Polar Engineering Conference, Kitakyushu, Japan, 26–31 May 2002; International Society of Offshore and Polar Engineers (ISOPE): Cupertino, CA, USA; Volume 3, pp. 190–197.
148. Berhault, C.; Guerin, P.; le Buhan, P.; Heurtier, J.M. Investigations on Hydrodynamic and Mechanical Coupling Effects for Deepwater Offloading Buoy. In Proceedings of the 14th International Offshore and Polar Engineering Conference, Toulon, France, 23–28 May 2004; International Society of Offshore and Polar Engineers (ISOPE): Cupertino, CA, USA; Volume 1, pp. 374–379. Available online: <https://onepetro.org/ISOPEIOPEC/proceedings-abstract/ISOPE04/All-ISOPE04/ISOPE-I-04-363/10313> (accessed on 11 September 2021).

149. Williams, N.A.; McDougal, W.G. Experimental Validation of a New Shallow Water Calm Buoy Design. In Proceedings of the 32nd International Conference on Ocean, Offshore and Arctic Engineering, Volume 1: Offshore Technology, Nantes, France, 9–14 June 2013; OMAE2013-11392; V001T01A070. The American Society of Mechanical Engineers (ASME): New York, NY, USA, 2013; pp. 1–6. [[CrossRef](#)]
150. Salem, A.G.; Ryu, S.; Duggal, A.S.; Datla, R.V. Linearization of Quadratic Drag to Estimate CALM Buoy Pitch Motion in Frequency-Domain and Experimental Validation. *J. Offshore Mech. Arct. Eng.* **2011**, *134*, 011305. [[CrossRef](#)]
151. Wang, F.; Chen, J.; Gao, S.; Tang, K.; Meng, X. Development and sea trial of real-time offshore pipeline installation monitoring system. *Ocean Eng.* **2017**, *146*, 468–476. [[CrossRef](#)]
152. Barltrop, N.D.P.; Adams, A.J. *Dynamics of Fixed Marine Structures*, 3rd ed.; Butterworth Heinemann: Oxford, UK, 1991.
153. Barltrop, N.D.P. *Floating Structures: A Guide for Design and Analysis-Volume 1*; Oilfield Publications Limited (OPL): Herefordshire, UK, 1998.
154. Chen, L.; Basu, B. Wave-current interaction effects on structural responses of floating offshore wind turbines. *Wind Energy* **2019**, *22*, 327–339. [[CrossRef](#)]
155. Newman, J. Wave effects on deformable bodies. *Appl. Ocean Res.* **1994**, *16*, 47–59. [[CrossRef](#)]
156. Newman, J. Absorption of wave energy by elongated bodies. *Appl. Ocean Res.* **1979**, *1*, 189–196. [[CrossRef](#)]
157. Newman, J.N.; Lee, C.-H. Boundary-Element Methods in Offshore Structure Analysis. *J. Offshore Mech. Arct. Eng.* **2002**, *124*, 81–89. [[CrossRef](#)]
158. Brebbia, C.; Dominguez, J. Boundary element methods for potential problems. *Appl. Math. Model.* **1977**, *1*, 372–378. [[CrossRef](#)]